THE UNIVERSITY
OF ADELAIDE
AUSTRALIA

Faculty of Engineering, Computer and Mathematical Sciences
SCHOOL OF MECHANICAL ENGINEERING

Ocean acoustic interferometry

DOCTORAL THESIS

12th October 2008

Author: Laura A. Brooks

Supervisor: Assoc. Prof. Anthony C. Zander [†]
Co-supervisors: Dr Peter Gerstoft [††]
                  Prof. Colin H. Hansen [†]
                  Dr Z. Yong Zhang [*]

[†]School of Mechanical Engineering, The University of Adelaide, Australia
[††]Marine Physical Laboratory, Scripps Institution of Oceanography, USA
[*]Defence Science and Technology Organisation, Edinburgh, Australia

Chapter 6

Experimental Active Ocean Acoustic Interferometry

Active source ocean acoustic interferometry (OAI) presents a number of advantages over the passive noise OAI technique described in Chapter 5, including the use of higher frequencies, which give sharper arrival peaks, as well as controllability and continuous monitoring. Greater knowledge of the contributing sources also means that more realistic simulated data can be produced. An active set of sources that surrounds the two points of interest could potentially achieve an isotropic source field. Due to the technical complexity of creating such a situation, the characteristics of, and results from, simpler active source configurations are investigated here: a source that is lowered vertically over the depth of the ocean water column, and a source that is towed horizontally along a straight line towards the array at a constant depth. Both of these source tracks are contained within the end-fire plane, which is defined as the plane containing the hydrophone array (i.e., the plane of the page in Figures 6.1 and 6.2(a)). These configurations have been examined theoretically and through simulation in Chapter 3.

Within this chapter cross-correlations between data recorded on hydrophones in an L-shaped array, and obtained using the two active source configurations, source lowering and towed source, are compared and contrasted

with cross-correlations of noise generated during the source lowering event by the ship from which the source was being controlled, and also with cross-correlations from a noise field dominated by shipping. Although recorded simultaneously, data from the active source being lowered, and from the ship during the lowering, can be analysed separately since the active source frequency range was 1200–2900 Hz, which is well above the 20–100 Hz frequency range in which noise generated by the ship dominated.

The active source experiments were performed in seas with a 2–2.5 m swell, residual effects from the passing of Tropical Storm Ernesto the day before. These conditions hindered controllability of the experiments, and therefore the movement of the source was not completely uniform. In addition, the swell would have caused the Green's function between two points to fluctuate more than usual, which would likely have had detrimental effects on the results obtained. Although the conditions were less than ideal, it was the only opportunity for the experimental work to be completed, since the extensive organisation and high costs associated with at-sea experiments ensures tight schedules, and an entire day of experimental time had already been lost during the storm. The various source configurations that were used are discussed theoretically in Section 6.1, and experimental results for each source type, from cross-correlation of data collected during the SW06 (Shallow Water 2006) sea trials, are compared and explained in Section 6.2.

A significant proportion of the work in this chapter has been submitted for publication in JASA [85].

6.1 Background

Consider the isovelocity waveguide depicted in Figure 6.1. The x, y and z directions are defined as the horizontal axis, the axis in-and-out of the page, and the vertical axis, respectively. Cross-correlation of the signals received

at A and B from a source at S yields

$$C_{AB}(\omega) = \rho_s^2 |S(\omega)|^2 G(\mathbf{r}_A, \mathbf{r}_S) G^*(\mathbf{r}_B, \mathbf{r}_S), \qquad (6.1)$$

where ω is frequency, $S(\omega)$ is the source spectrum, ρ_s is the density of the medium, $G(\mathbf{r}_\psi, \mathbf{r}_S)$ is the Green's function between the source S, and receiver ψ, and * denotes the complex conjugate.
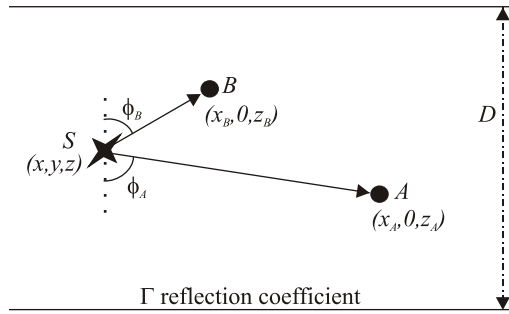

Figure 6.1: Source-receiver geometry and notation. Receivers A and B define the $y = 0$ plane, and source S is located within the waveguide of depth D, but is otherwise unrestricted.

The sum of the cross-correlations over a set of sources is, from Eq. (3.4):

$$C_{AB}(\omega) = |\rho_s S(\omega)|^2 n \int G(\mathbf{r}_A, \mathbf{r}_S) G^*(\mathbf{r}_B, \mathbf{r}_S)\, dA, \qquad (6.2)$$

where n is the number of sources per unit length (line source), area (planar source), or volume (volume source), and the integral is over the source line, plane or volume.

The cross-correlation of data from four source types are considered here:

1. active source lowered vertically in the end-fire plane over the depth of the waveguide, modelled as a vertical line of sources, $\int dA \sim \int dz$;

2. active source towed in the end-fire plane towards the array at a constant depth z, modelled as a horizontal line of sources, $\int dA \sim \int dx$;

3. stationary ship source, modelled as an "extended" point source, $\int dA \sim \int \delta(x,y)dA$; and

119

4. ship dominated ambient noise field, modelled as a horizontal plane of sources at a shallow depth z, $\int dA \sim \iint dx dy$.

The oscillatory characteristics of the integral in Eq. (6.2) allow it to be solved via the method of stationary phase [68]. The integral is estimated in the neighbourhood of the stationary points, which are the points where the partial derivative of the difference in path lengths to each receiver in the direction of the line integral is equal to zero (i.e., the extrema of the cross-correlation function exponential), and the contributions are then summed over all stationary points. The stationary phase solution to Eq. (6.2), can be derived from Eq. (3.16) for a vertical line of sources in the end-fire plane, source type 1, assuming 3D-wave propagation, as

$$
C_{AB}(\omega) = in|S(\omega)|^2
$$
$$
\times \sum_{z_s} \left(\frac{\Gamma^{b_A + b_B} \rho_s^2 \, G_f\left(R\left(z_s\right)\right)}{\sin \phi_s} \sqrt{\frac{\xi(z_s)c}{-8\pi i \omega}} \right); \tag{6.3}
$$

and from Eq. (3.29) for a horizontal line of sources in the end-fire plane, source type 2, as [13, 30]

$$
C_{AB}(\omega) = in|S(\omega)|^2
$$
$$
\times \sum_{x_s} \left(\frac{\Gamma^{b_A + b_B} \rho_s^2 \, G_f\left(R\left(x_s\right)\right)}{\cos \phi_s} \sqrt{\frac{\xi(x_s)c}{-8\pi i \omega}} \right); \tag{6.4}
$$

where Γ is the bottom reflection coefficient, b_ψ is the number of bottom reflections for the path to ψ, where $\psi = A$ or B, R is the total distance that a particular wave travels, $G_f(R) = \frac{e^{ikR}}{4\pi R}$ is the 3D Green's function within a homogeneous medium, ϕ_s is the acute angle between the ray path and the vertical (see Figure 6.1), $\xi = \frac{1}{L_B} - \frac{1}{L_A}$, L_ψ is the length of the given path between the source, S, and receiver, ψ, c is the speed of sound in the medium, and z_s and x_s are the stationary points for the vertical and horizontal configurations respectively. The term on the RHS of Eq. (6.4) is termed the phase and amplitude shaded Green's function, because it is the Green's function convolved with phase and amplitude terms. The 3D

Green's function within a homogeneous medium, $G_f(R)$, differs from the true Green's function between A and B, $G(R)$, in that it does not incorporate the path dependent amplitude reduction due to bottom interactions, as explained in Section 3.1. The relationship between them is, from Eq. (3.6),

$$G(R(x_s)) = \Gamma^{b_s} G_f(R(x_s)), \tag{6.5}$$

where b_s is the number of bottom reflections for the arrival between A and B, corresponding to the stationary point x_s.

For a point source, source type 3, Eq. (6.2) simplifies to

$$C_{AB}(\omega) = \frac{|\rho S(\omega)|^2 \Gamma^{b_A+b_B} e^{ik(L_A-L_B)}}{16\pi^2 L_A L_B}. \tag{6.6}$$

In general $L_A - L_B$ is less than the inter-receiver path length (triangle inequality theorem) and therefore arrival times are underestimated. Although the stationary ship source is larger than a point source, the area of integration in Eq. (6.2) is small, and therefore it is not a Green's function estimate. However, if the ship is close to the stationary path it may provide a good approximation.

The structure of the ship noise cross-correlations will only converge to the arrival structure of the Green's function when the cross-correlation time is averaged over several ship tracks, hence the consideration of ship dominated ambient noise, source type 4. For a horizontal plane of sources the stationary phase solution to Eq. (6.2) is, from Eq. (5.5):

$$C_{AB}(\omega) = in|S(\omega)|^2 \sum_{\chi_s} \left(\frac{\Gamma^{b_A+b_B} c\rho_s}{2\omega \cos\phi_s} G_f(R(\chi_s)) \right), \tag{6.7}$$

where χ_s are the horizontal planar stationary points.

The solutions for the line sources, Eq. (6.3) and Eq. (6.4), are of the same form, differing only in the trigonometric function of the acute ray angle ($\frac{1}{\sin\phi_s}$ term for a vertical line source, and $\frac{1}{\cos\phi_s}$ for a horizontal line source), and the locations at which stationarity occurs. The difference in source dimensionality (1D line source distribution versus 2D planar source

121

distribution) is responsible for the increased complexity of the line source solutions when compared to a 3D Green's function.

For each source configuration the summed cross-correlation produces an amplitude and phase shaded Green's function (i.e., a standard Green's function that is multiplied by amplitude and phase dependent weighting coefficients). The amplitude shading consists of constant (n, ρ_s, c, π, and numeric factors), path dependent ($\Gamma^{b_A+b_B}$, ϕ_s, L_A, and L_B), and frequency dependent (ω and $S(\omega)$) terms.

As explained in Section 3.1.1, the i/ω factor in Eq. (6.7) can be corrected for by using the time-derivative of the cross-correlations [11, 13, 15], and the $i/\sqrt{-i\omega}$ factor in Eq. (6.4) and Eq. (6.3) can be corrected for with a $\pi/2$ phase shift, and a fractional time derivative of 0.5 order [13]. This should yield a result with correct arrival times.

Deconvolution of the source term, $S(\omega)$, from the cross-correlations can present difficulties and hence the Green's functions are instead convolved with the source term, yielding a source shaded Green's function, before comparisons with the phase corrected empirical cross-correlations are made. The constant amplitude shading factors need not be considered since all data are normalised before comparing. Due to their variability, the path dependent amplitude factors are difficult to correct for, and hence correct arrival times but incorrect amplitudes are expected when comparing the phase corrected cross-correlations and the source shaded Green's function.

As discussed in Section 3.1.3, spurious arrivals, defined as peaks in the cross-correlation function at times not corresponding to Green's function path travel times, can occur for each source geometry. For the horizontal planar and line configurations, spurious arrivals will result due to stationary-phase contributions from cross-correlations between waves that initially undergo a surface reflection and ones that do not. For an isovelocity water column, one wave departs at an angle of ϕ from the horizontal, and the other departs at an angle of $-\phi$ [15]. If the depth of the plane of sources is reduced, the spurious peaks converge to the same time delay as

the true Green's function paths; however, they are π out of phase and will therefore result in shading of the Green's function [15]. For the vertical line configuration, spurious arrivals will result when the line integral does not extend to infinity.

6.2   Experiment

6.2.1   Data collection

Acoustic data for OAI were collected on the L-shaped SWAMI32 array, with the geometry shown in Figure 6.2(a). Hydrophones 1–12 (H-1–H-12) constitute the vertical line array (VLA), with H-11 and H-12 co-located, and H-13–H-32 constitute the horizontal line array (HLA).

Data from four source types were recorded:

1. 1200–2900 Hz linear frequency modulated (LFM) source lowered from 9.8–60 m at a constant rate of 1 m/min, at a location 466 m from the VLA, in the end-fire plane (vertical line source: see source lowering geometry and location in Figure 6.2(a)–(b));

2. 1200–2900 Hz LFM source held at 10 m depth towed at 1 knot toward the array in the end-fire plane, from a distance of 1.5 km from the VLA, to a location mid-way between H-16 and H-30 (horizontal line source: see towed source geometry and location in Figure 6.2(a)–(b));

3. 20–100 Hz noise generated by the deployment vessel R/V *Knorr* (location shown in Figure 6.2(a)) during the source lowering experiment; and

4. 20–100 Hz ship dominated ambient noise (horizontal planar source).

A horizontal hyperbolic towed source was theoretically described in Section 3.3. Data from two hyperbolic towed sources were collected during the experiments, but are not analysed in detail here because they showed less
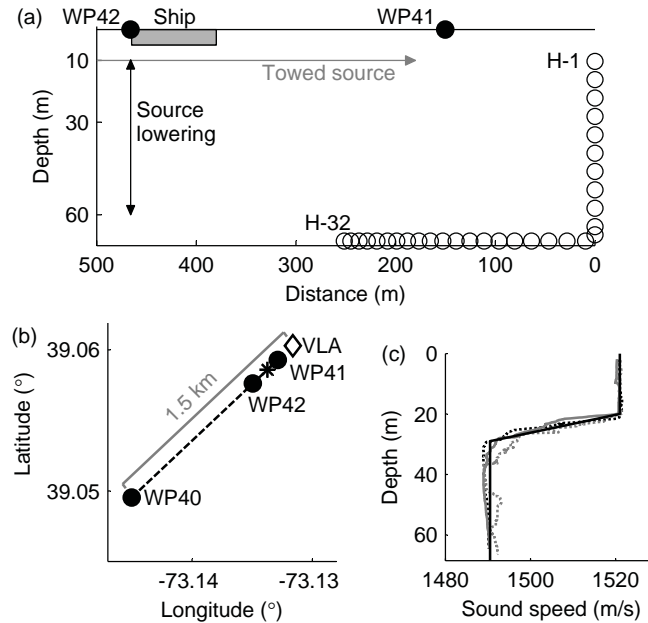
Figure 6.2: (a) Source and receiver geometries: SWAMI32 hydrophones shown as circles, where H-11 and H-12 are collocated at the VLA bottom, and ship location is during source lowering. (b) Plan view of array with VLA labelled, asterisk marking far end of HLA, and source geometries showing where the source is towed from WP40 to WP41, and lowered at WP42. (c) SSPs from CTDs 42–44, shown as black dotted, grey solid and grey dotted lines respectively. Assumed SSP for modelling is overlaid in a black solid line.

resemblance to the acoustic Green's function than the other two source configurations. Plans for future work involving the hyperbolic source data are described in Section 8.2.3.

The ship dominated noise data, source type 4, were collected during Tropical Storm Ernesto over the entire day of September 2, and data from source types 1–3 were collected on the afternoon of September 3 2006. There was little wind, but there was a residual swell of 2–2.5 m, as well as strong inhomogeneity in the ocean due to the previous day's storm. These made it difficult to move the active source along the desired tracks. Sound speed profiles (SSPs) were recorded from CTD42 (conductivity, temperature, depth measurement 42) at waypoint 40 (WP40), CTD43 at WP42,

and CTD44 near WP41, before, during, and after the September 3 experiments respectively. These three SSPs are shown in Figure 6.2(c), along with a simpler SSP that is assumed for simulations.

On September 2 several of the SWAMI32 channels switched, as described in detail in Chapter 7. Corrections for this were applied to the relevant data presented here.

6.2.2   Data analysis

Active source data from all hydrophone pairs were bandpass filtered to 1200–2900 Hz, and ship noise data were bandpass filtered to 20–100 Hz. The ship dominated ambient noise data were then one-bit normalised in the time domain (i.e., amplitude was discarded but sign, or phase, of the waveform was retained), and normalised by a smooth version of their amplitude spectra in the frequency domain, as discussed in detail in Section 5.4. The active source and stationary ship data did not require normalisation since variations in the source amplitude and phase characteristics were negligible throughout each experiment.

The preprocessed data were cross-correlated over short time intervals, and then summed over the period of collection for each source type. As specified in Section 6.1, a raw summed cross-correlation (see Eqs. (6.3), (6.4) and 6.7) yields a phase and amplitude shaded Green's function approximation. The phase shading and frequency dependent components, as explained in Section 6.1, were corrected for by evaluation of the time derivative for source type 4, and by using a $\pi/2$ phase shift and a fractional time derivative for source types 1 and 2. Although source type 3 also has a phase shift, it is geometry dependent, due to the length discrepancy in the exponential of Eq. (6.6), and therefore no correction factors are applied to the stationary ship noise data. Inclusion of the appropriate phase correction is, henceforth, implicit in the term 'cross-correlation'.

The cross-correlation sum is termed the *empirical Green's function approximation* (EGFA). The EGFA envelopes of the cross-correlations be-

tween H-30 and all other hydrophones are shown in Figure 6.3 for the four source types in Section 6.2.1. Simulated direct, surface reflected, surface-bottom reflected (VLA only), and surface-bottom-surface reflected path travel times, which were determined using OASES [49], are overlaid as dotted lines for comparison. The simulations use the assumed SSP of Figure 6.2(c) and sediment properties estimated from nearby sediment grab sample data [73]. The ship dominated ambient noise results, shown in Figure 6.3(d), have both causal and acausal components, that is, peaks at positive cross-correlation time corresponding to signals travelling from left to right from the perspective of Figure 6.2(a), as well as peaks at negative time corresponding to signals travelling from right to left. This is because the sound comes from all directions, though only the first 0.05 s of the acausal signal is shown here. The other three configurations, shown in Figure 6.3(a)–(c), have sources travelling in one direction only, from left to right from the perspective of Figure 6.2(a), and therefore produce a one-sided EGFA. The stationary ship EGFA (c) and ship dominated ambient noise EGFA (d) show broader peaks than the active source results, (a) and (b), due to the lower frequencies, 20–100 Hz, of the ship noise compared to the 1200–2900 Hz active source frequencies.

The EGFA envelopes for all source types, as shown in Figure 6.3, exhibit distinct peaks at times agreeing with the simulated direct inter-hydrophone travel times. The times corresponding to these peaks are compared in Figure 6.4. Minimal variations are seen for all HLA hydrophone combinations, though the stationary ship peak times (c) are generally slightly less than the others, which is due to the discrete nature of the source location. No signals from the source pass through the location of the first hydrophone, on their way to the second hydrophone, with a direct path in between.

The variation in the EGFA peak times corresponding to the direct arrivals between the hydrophones are notably larger for the VLA hydrophones. Due to their location, the VLA hydrophones are more sensitive to environmental variations and more susceptible to movement than their HLA
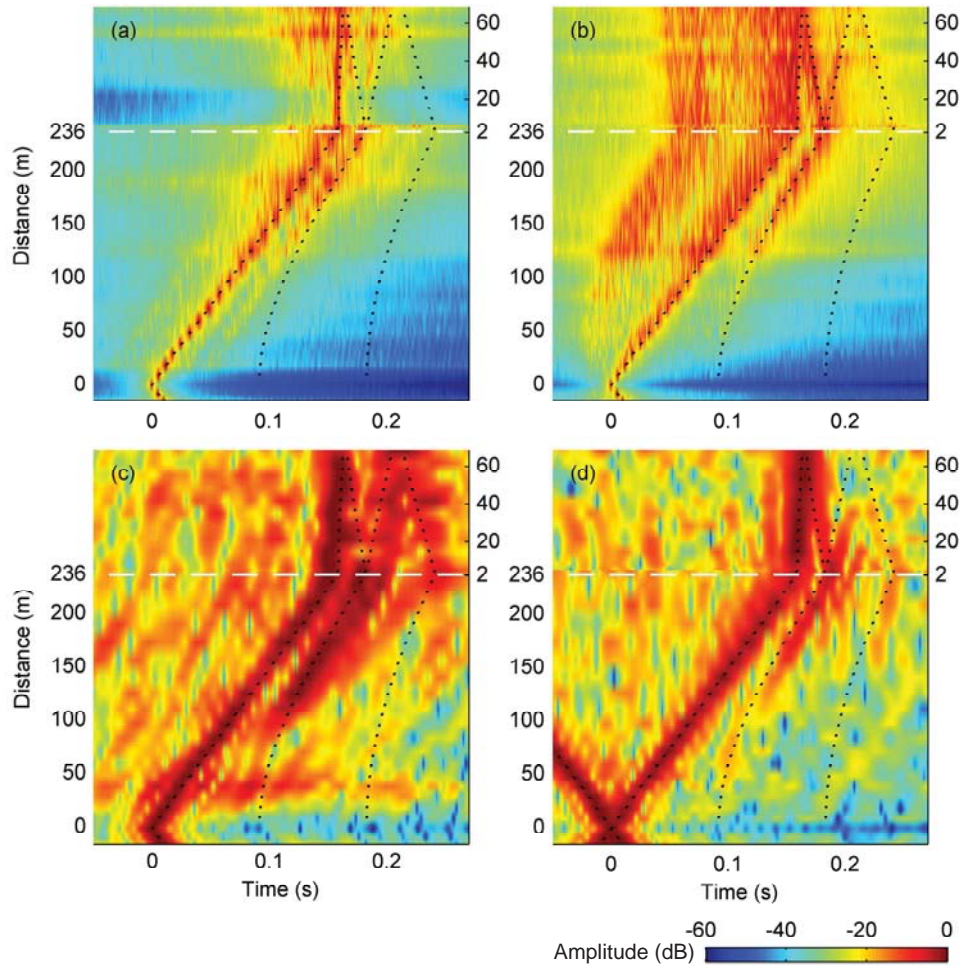
Figure 6.3: EGFA envelopes (dB relative to maximum value) between H-30 and all other hydrophones, overlaid with simulated travel times shown as black dotted lines, for: (a) source lowered vertically from 9.8–60 m, (b) source towed horizontally towards the array, (c) noise generated by R/V *Knorr* during the source lowering, and (d) ship dominated ambient noise. The traces below the dashed white line are from cross-correlations with HLA hydrophones; their distance from H-30 is on the left axis. The upper traces are from cross-correlations with VLA hydrophones; their vertical distance from the seafloor is on the right axis. A lower threshold of -60 dB has been applied to the amplitude.
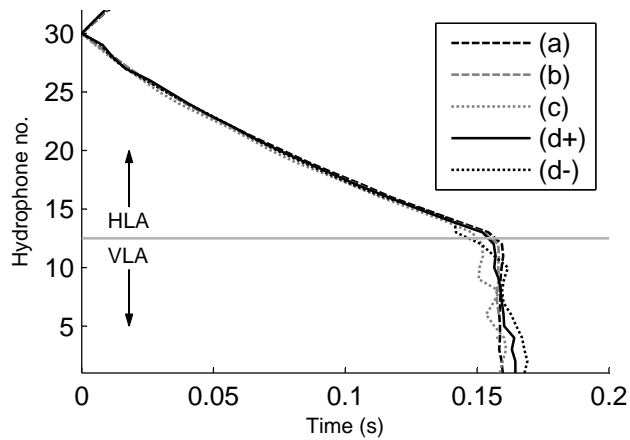
Figure 6.4: Times corresponding to the direct path arrival EGFA envelope peaks of Figure 6.3 as a function of hydrophone number: (a) source lowering, (b) towed source, (c) stationary ship, (d+) causal ship dominated ambient noise, and (d-) acausal ship dominated ambient noise.

counterparts.

The EGFA peaks in Figure 6.3 that correspond to the surface reflected arrivals show more variation than the direct path peaks. The towed source and ship dominated ambient noise results, shown in Figure 6.3(b) and (d) respectively, show a surface reflection peak for all hydrophones more than 40 m from H-30. The source lowering results, shown in Figure 6.3(a), exhibit peaks at slightly early times for hydrophones more than 150 m from H-30. For hydrophones less than 150 m away, peak times diverge from the simulated values. The stationary ship results, shown in Figure 6.3(c), show an arrival peak for HLA hydrophones at ranges greater than 100 m, but the VLA results are not so clear.

The greater the complexity of the acoustic travel paths, the more detrimental any inaccuracies in the simulated environment would have been. For this reason, the EGFA peaks in Figure 6.3 that correspond to the surface-bottom reflected arrivals between H-30 and the VLA hydrophones, show greater variation from the simulated travel times than the EGFA peaks that correspond to the lower order paths.

The amplitudes of the EGFA peaks are greatest, relative to the background noise, for the active source cross-correlations. This is due to high levels of coherently propagating noise which result from the close proximity of the source and the even distribution of the source over the active source line integrals.

In order to more fully explain the EGFA envelopes of Figure 6.3, OAI data for one hydrophone pair, H-30 and H-5, will be examined in detail for each of the four sound sources in the coming sections.

Vertical source lowering

The theoretical vertical line source description in Section 6.1 assumes a set of sources that is uniformly distributed along the line, as explained in Section 3.1. The source was slowly lowered vertically, but was only at one location at any given time. The line source configuration was therefore obtained by cross-correlating data over short time intervals, and summing these cross-correlations. Thus, while the cross-correlations as a function of depth are initially described here, it is the sum of the cross-correlations over all source depths that were used to approximate the EGFA in Figure 6.3(a). The EGFA approximation could instead have been obtained by one single cross-correlation of the data collected from the entire source lowering, but this would have been computationally less efficient, and would not have allowed for analysis of the cross-correlation as a function of source depth.

The geometric set-up of the source lowering, as well as the stationary point travel paths and surface and bottom sources that converge to the stationary points for H-5 and H-30, are shown in Figure 6.5. As explained in Section 3.1.2, a source should ideally be lowered through the water column and sediment, but due to experimental restrictions the source could only be lowered from 9.8–60 m, the deeper limit being approximately 8.5 m above the seafloor.

Cross-correlations of 100 s duration between H-5 and H-30 are shown as a function of source depth for experimental data and data simulated
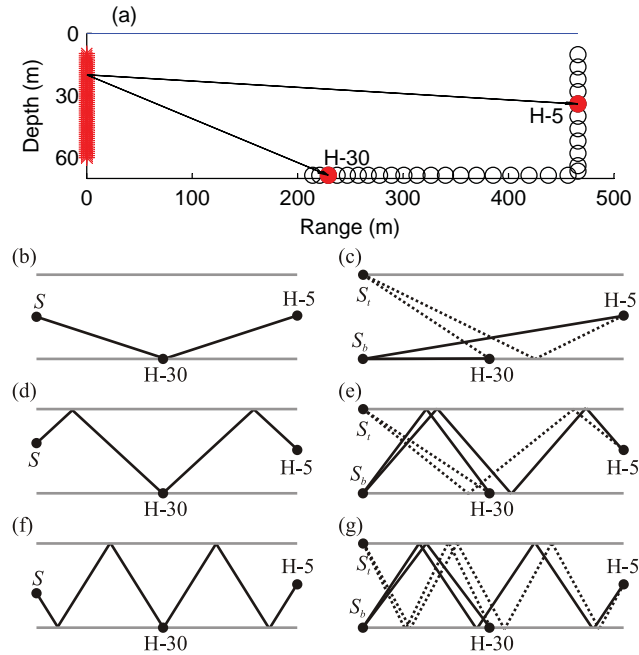
Figure 6.5: Source lowering. (a) Source (far left) is lowered from 9.8–60 m, and signals are recorded on H-5 and H-30, which are shown as solid red circles. (b)–(g) Source-receiver geometry and stationary point paths for (b) direct, (d) surface, and (f) surface-bottom paths between the two hydrophones. (c), (e), and (g) are the surface (S_t) and bottom (S_b) source to receiver paths that converge to the stationary point paths in (b), (d), and (f) respectively.

using OASES in Figure 6.6(a) and Figure 6.6(b)–(c) respectively. Cross-correlation peaks occur at the time differences between paths from the source to each hydrophone. For example, consider the direct path from the source to H-30 and the bottom reflected path to H-5 shown in Figure 6.5(b)–(c). The simulated time differences between these paths for sources at the top or bottom of the waveguide, as shown in Figure 6.5(c), are depicted in Figure 6.6 as the first set of solid red circles at 0.16 s. The curve of cross-correlation peaks connecting these circles, and best seen in Figure 6.6(c), corresponds to the time difference between these paths for each source depth. The time difference increases to a maximum, also called the stationary point, which is depicted as a solid green circle in Figure 6.6(c),

at 40 m depth. This stationary point occurs when the path to the second hydrophone, H-5, passes through the first hydrophone, H-30, as shown in Figure 6.5(b). The two paths have a travel time difference equivalent to the time taken to travel the distance between H-30 and H-5, and therefore correspond to the direct arrival, where arrival refers here, and henceforth, to the travel path between the two hydrophones, not the travel path from the source to one of the hydrophones.

The surface and surface-bottom reflected arrivals between two hydrophones can be analysed in a similar way to the direct arrival just discussed, as shown in Figure 6.5 and marked with solid circles in Figure 6.6.

Consider the four paths that converge as the source location moves towards the surface of the waveguide, to the direct path from the source to H-30, and bottom reflected path from the source to H-5. The convergence point is shown as the first circle, (c) S_t, in Figure 6.6(c). The cross-correlations near this point are reproduced in Figure 6.7, along with schematics of the four paths that converge at this point. The cross-correlations of paths (b) and (e) are in phase with one surface reflection each, and their amplitudes are equal in amplitude at the convergence point. Since the path length difference of (b) increases as the source location moves towards the surface, the path length difference of (e) decreases as the source location moves towards the surface, and their rates of change with source depth are also the same, the cross-correlation peaks due to these combinations transfer smoothly from one path combination to the other at the convergence point, and therefore there is no spurious arrival. A similar argument holds for paths (c) and (d) and all other sets of paths at the waveguide surface and bottom, and therefore no peak should occur at any of these convergence points when the cross-correlations are summed. However, if the amplitude of the surface or bottom reflection coefficient is not unity, there will be discontinuities in the correlation when the total number of surface and bottom reflections of the two converging paths is not identical. Truncation errors due to the non unity reflection coefficients at the
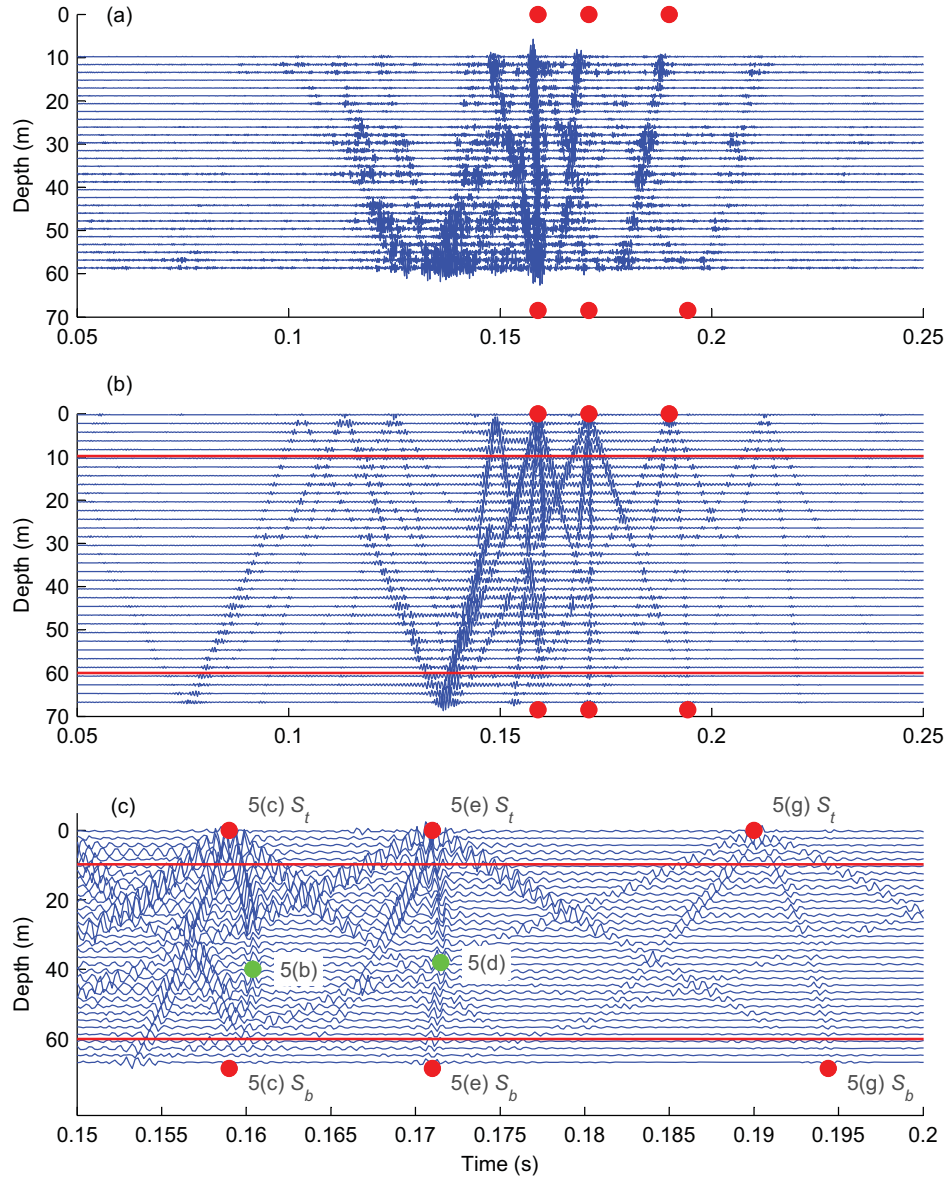
Figure 6.6: Cross-correlated data versus source depth: (a) experimental, (b) simulated, and (c) extract of simulated data. The solid red circles correspond to time differences between the surface and bottom source paths to H-5 and H-30. These paths are shown in Figure 6.5(c), (e) and (g). The solid green circles in (c) correspond to the direct and surface reflection stationary points in Figure 6.5(b) and (d).

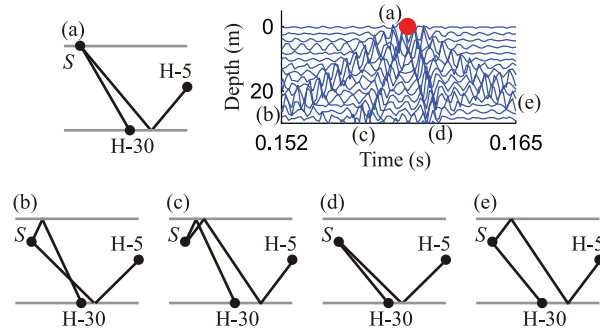bottom of the waveguide are discussed in Section 3.1.2.

Figure 6.7: View of part of the simulated cross-correlations from Figure 6.6(c), showing the direct path to H-30 and bottom reflected path to H-5 surface convergence point (a), and the four sets of paths that converge to this point as the source moves towards the surface (b)–(e).

The simulated and experimental data of Figure 6.6 differ in three main ways.

1. The experimental data are not as sharp, likely due to 2–2.5 m swell, which caused both the source and waveguide depth to oscillate throughout the lowering event.

2. There are variations in amplitudes for different path combinations, with some path combinations more affected than others. Likely reasons are that the bottom reflection coefficient, or sediment properties, of the simulation are only an estimation, and that due to waves, the surface reflection was not specular. Most paths depend on some power of surface and bottom reflection, as can be seen from Eqs. (6.3–6.7), and higher order paths are more sensitive to these reflection coefficients.

3. Peak times differ slightly, likely due to slight mismatch in sound speed profile and water column depth between the experimental and simulated environments.

The unity surface reflection and the sediment properties that were assumed for the simulations are only approximations. Since the differences between the cross-correlation amplitudes of the simulated and experimental data, item 2, are due mainly to variations in the environment from that assumed, these differences could potentially be used to invert for the actual surface and bottom reflection coefficients.

The cross-correlations were summed over depth. The experimental summed data, $\sum C$, are compared with both simulated summed data and the source shaded Green's function in Figure 6.8.
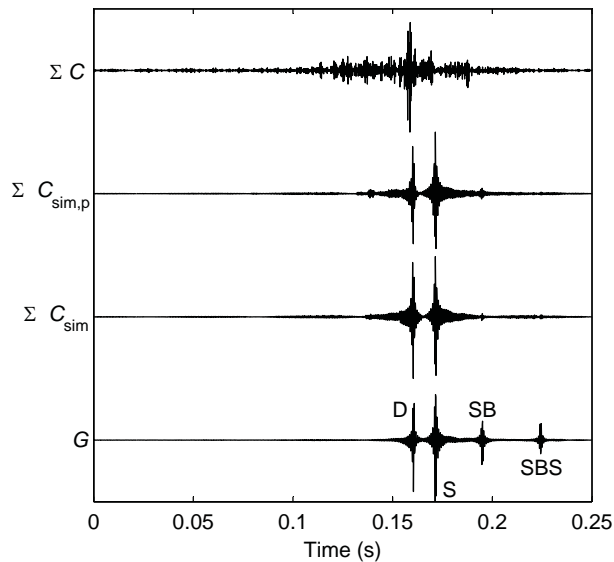

Figure 6.8: The sum of the H-5 and H-30 cross-correlations from the source lowering experiment, $\sum C$, is compared to the simulated cross-correlations summed from 9.8–60 m, $\sum C_{\mathrm{sim,p}}$, the simulated cross-correlations summed over the entire waveguide, $\sum C_{\mathrm{sim}}$, and the simulated source shaded Green's function, G. The Green's function shows direct, D, surface, S, surface-bottom, SB, and surface-bottom-surface, SBS, paths.

The sum of the simulated data over the waveguide, $\sum C_{\mathrm{sim}}$, shows direct, surface reflected, and surface-bottom reflected peaks at correct Green's function, G, time lags in Figure 6.8. The amplitudes are different, as explained in Section 6.1. The significantly smaller amplitude of the surface-

134

bottom reflected path in $\sum C_{\text{sim}}$ when compared to the Green's function is due to losses from the large number of boundary interactions. The Green's function for this path has only one surface and one bottom reflection, but the two paths that are cross-correlated have 3 surface and 4 bottom reflections between them. This difference in amplitude due to bottom interactions can be seen by comparing Eq. (6.3) and Eq. (6.5). The sum of the simulated data from 9.8–60 m only, $\sum C_{\text{sim,p}}$, has small spurious peaks around 0.14 s, which is earlier than the direct arrival. These are mainly because the cross-correlation arrivals that should converge and cancel with other paths at the seafloor do not converge due to the 8.5 m gap in cross-correlations at the waveguide bottom.

The experimental summed cross-correlation shows peaks at the direct arrival time as well as times slightly less than the surface reflected and surface-bottom reflected arrivals. The main cause of discrepancies in the secondary path peaks can be explained by considering Figure 6.6. The cross-correlations from the travel paths containing the surface and surface-bottom stationary points, the second and third set of solid red circles respectively, are faint in the simulated data, but are not visible in the experimental data, likely due to the source distribution not being completely even, and the environment, in particular the water depth and sound speed profile, constantly changing throughout the source lowering. The summed data are therefore dominated by the stronger peaks from the surface source convergence points that are slightly earlier, that is, the second and third solid red circles at the surface. The amplitude of the surface reflection coefficient is likely less than unity and this causes contributions near the surface convergence points, shown as solid red circles in Figure 6.6.

Horizontal towed source

Following the same reasoning as for the vertical source lowering in Section 6.2.2, to obtain a line source, short time cross-correlations were summed over the time during which the source was towed from WP40 to WP41. The

theory assumes a source that extends out to infinity. Stopping the source suddenly at a finite location can therefore result in spurious arrivals due to the presence of end-effects from cross-correlations at the end point that would cancel with cross-correlations from sources at slightly greater distances if the tow extended further. In order to minimise these end-effects, a tapered cosine window, with length 5% of the total length over which the source was towed, was therefore applied to the amplitude of the cross-correlations from the furthest sources. The H-5 and H-30 100 second long cross-correlations are shown in Figure 6.9 as a function of range for experimental data as well as data simulated using OASES. The direct, surface reflection, and surface-bottom reflection stationary points, which are the points at which the time of arrival of the cross-correlation peaks are local maxima, are difficult to see at this scale, and are therefore circled for clarity. The corresponding stationary point paths are shown in Figure 6.10(a)–(c). The stationary points occur within the first few hundred metres; the cross-correlation peak times increase rapidly to these points, as can be seen in Figure 6.9, and then asymptote towards a far-field fixed value. The towed source configuration has more than one source satisfying each stationary phase condition (i.e., more than one stationary point). The grey circles in Figure 6.10(a)–(c) are higher order source locations that emit signals that pass through the first hydrophone, H-30, and are then received on the second hydrophone, H-5. Since these signals experience more boundary interactions before being received at each hydrophone, their amplitudes are much smaller, and they are therefore not visible in Figure 6.9.

Figure 6.10(d)–(f) are stationary phase geometries where one wave departs at an angle of ϕ from the horizontal, and the other departs at an angle of $-\phi$. These source paths yield spurious arrivals, as explained in Section 6.1, and will be examined in more detail shortly.

The experimental summed cross-correlations over range, $\sum C$, are compared with the simulated summed cross-correlations, $\sum C_{\text{sim}}$, and the simulated source shaded Green's function, G, between H-30 and H-5 in Fig-
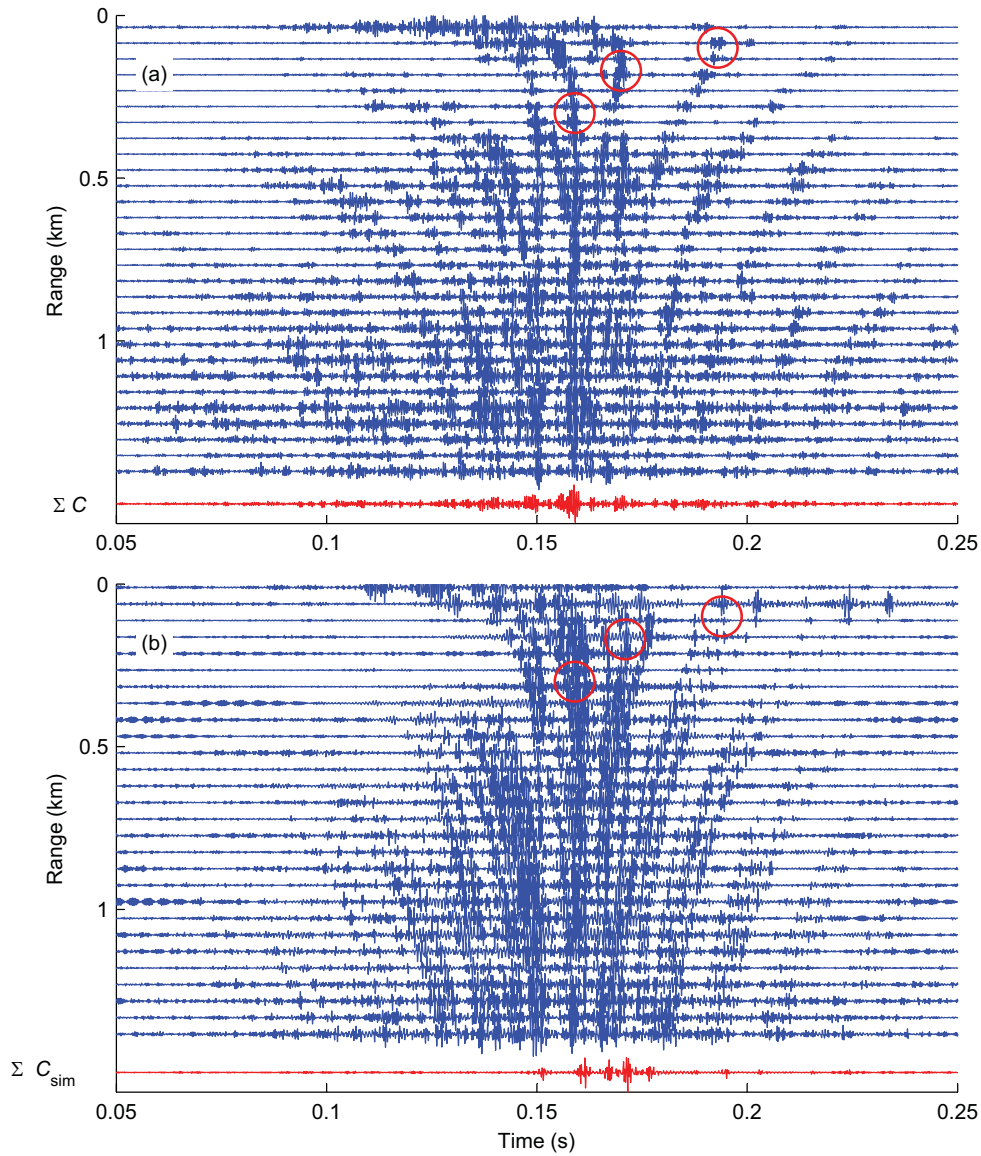
Figure 6.9: Cross-correlated towed source data, (a) experimental and (b) simulated, as a function of range (0–1.4 km) from H-30. The summed cross-correlations, $\sum C$ and $\sum C_{sim}$ respectively, are at the bottom of each plot.
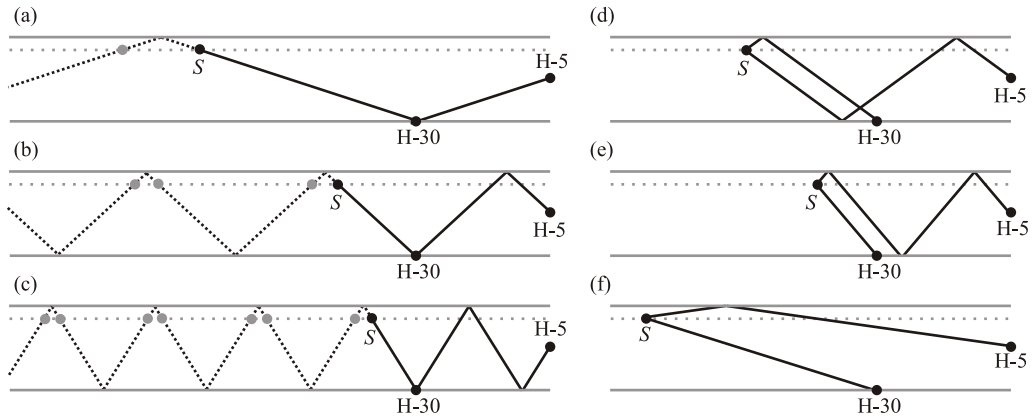
Figure 6.10: Source-receiver geometry and stationary point paths for (a) direct path, (b) surface reflection path, and (c) surface-bottom reflection path. The grey circles represent weaker stationary points. (d)–(f) Stationary phase geometries that yield spurious arrivals.

ure 6.11. The simulated cross-correlation sum shows direct, D, surface reflected, S, and surface-bottom, SB, arrival peaks at correct lag times. The experimental data have stationary points, circled in Figure 6.9(a), that yield arrival peaks at times slightly less than the simulated direct and surface reflected arrivals, as shown in Figure 6.11. This is likely due to mismatch between the experimental and simulated water depths and sound speed profiles. The experimental summed cross-correlation also has a higher noise background, which is likely due to convergence difficulties near zero range, where the data are very sensitive to the tapering method and the chosen physical end point.

Both the experimental and simulated cross-correlation sums exhibit numerous high amplitude spurious arrivals. For example, consider the two spurious arrivals, X2 and X3, that are visible in the summed simulated cross-correlations shown in Figure 6.11, before and after the surface reflected arrival, S. These spurious arrivals are due to the stationary phase paths shown in Figure 6.10(d)–(e).

The arrivals and stationary points that create these peaks are visible in Figure 6.9(b). Peaks corresponding to the time difference in the direct
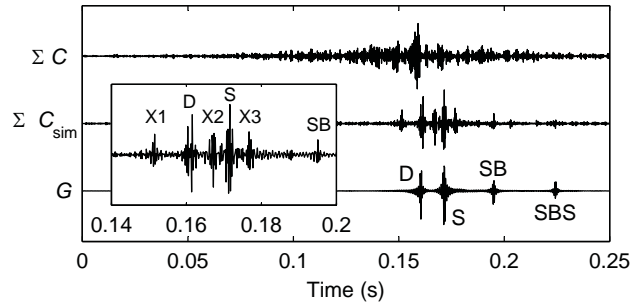
Figure 6.11: Sum of the H-5 and H-30 cross-correlations from the towed source experiment, $\sum C$, is compared to the simulated summed cross-correlations, $\sum C_{\mathrm{sim}}$, and the simulated source shaded H-5–H-30 Green's function, G. The Green's function shows direct, D, surface, S, surface-bottom, SB, and surface-bottom-surface, SBS, paths. An enlarged view of $\sum C_{\mathrm{sim}}$ from 0.14–0.2 s, showing inter-hydrophone arrivals D, S, and SB, and spurious arrivals X1–X3, is inset.

path to H-30 and the bottom-surface reflected path to H-5, with the surface reflection stationary point at 0.17 s circled, are flanked by a set of arrivals at slightly earlier and later times. These spurious arrivals, which are due to the cross-correlation of a wave that initially undergoes a surface reflection with one that does not, have stationary points corresponding to the geometry of Figure 6.10(d) and (e), and are labelled X2 and X3 respectively in the summed cross-correlations of Figure 6.11.

A significant peak, X1, is apparent in both the experimental and simulated cross-correlations at 0.15 s, which is prior to the direct path, D, arrival. This spurious arrival is due to a stationary phase contribution from the cross-correlation of the direct path to H-30 and surface reflection to H-5, as shown in Figure 6.10(f). The peak in the simulated and experimental data exist only in this varying SSP environment. Simulated cross-correlations for a 1500 m/s isovelocity waveguide with the same geometry do not show this peak, because such a stationary phase geometry does not exist when considering straight line paths only. The schematic of straight line paths in Figure 6.10(f) comes close to, but does not satisfy, the equal departure angle requirement; the path to H-5 always departs the source at an angle

closer to the horizontal than the path to H-30.

Stationary ship noise

The cross-correlated data from the stationary ship varied little with time, as can be seen in Figure 6.12. Since the source volume is small, the signals received by the hydrophones will be directionally biased, and hence a good estimate of the Green's function is not expected. However, cross-correlation of the ship data during this time does give a multi-path result that looks similar to the Green's function, except that the arrival *structure* does have path dependent inaccuracies. The times tend to be a little early due to the stationary phase path geometries not existing for any of the source locations within the small ship source volume.
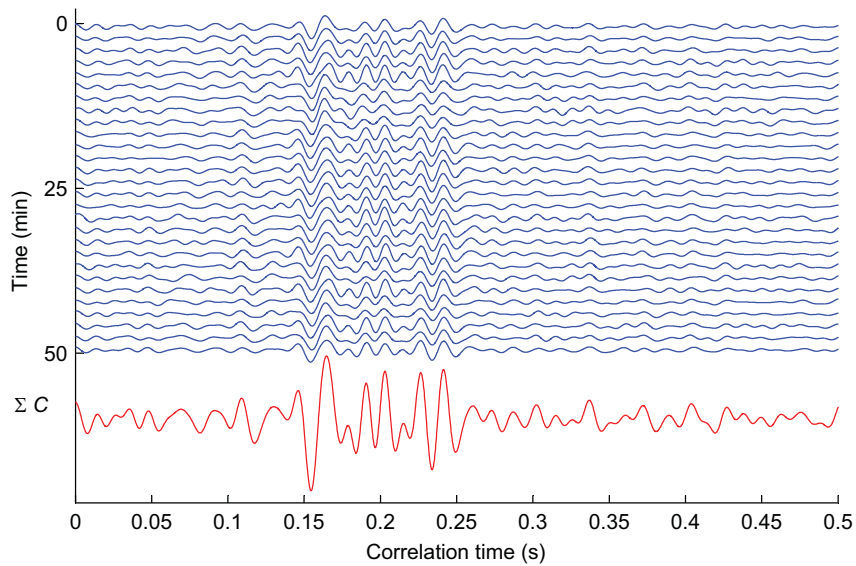
Figure 6.12: Cross-correlations of H-30 and H-5 data from the stationary ship as a function of time during the source lowering event. The sum of the cross-correlations, $\sum C$, is shown underneath.

Ship dominated ambient noise

The structure of ship noise cross-correlations will only converge to that of the true Green's function if either the ship moves along the end-fire direction, or the cross-correlations are averaged over many ship tracks that pass through the end-fire plane. Ship dominated ambient noise, which was investigated in greater depth in Chapter 5, meets the second of these criteria. It was modelled in Section 6.1 as a horizontal planar near-surface source. However, at any one time the signals tend to be dominated by one or two nearby ships, and hence cross-correlation must be performed over a sufficiently long period, here the entire day of September 2, such that several ship tracks that pass through the end-fire plane are included. The cross-correlation function, consisting of many cross-correlations that are each 100 s long, changes continuously throughout the day of September 2, as shown in Figure 6.13. High amplitudes at the direct travel time of ± 0.16 s indicate the presence of a ship near the end-fire plane, whilst high amplitudes at lesser times are contributions from ships closer to broadside (the direction horizontally perpendicular to the array). As an example, from 16–20 Z the acausal cross-correlation has negligible amplitude, suggesting a left-side dominant noise field from the perspective of Figure 6.2(a). From 20–24 Z a high amplitude peak is seen to move from -0.08 to -0.14 s, suggesting the presence of a ship that is moving towards the end-fire plane to the right of the array, again from the perspective of Figure 6.2(a). The causal and acausal direct path signal between H-5 and H-30 only emerges clearly after summation of the noise field over the whole day, $\sum C$, as can be seen in Figure 6.13.

6.3   Conclusion

Empirical Green's function approximations determined from two active source configurations, a vertically lowered source and a horizontally towed source, were compared with EGFAs from a stationary ship at a single end-
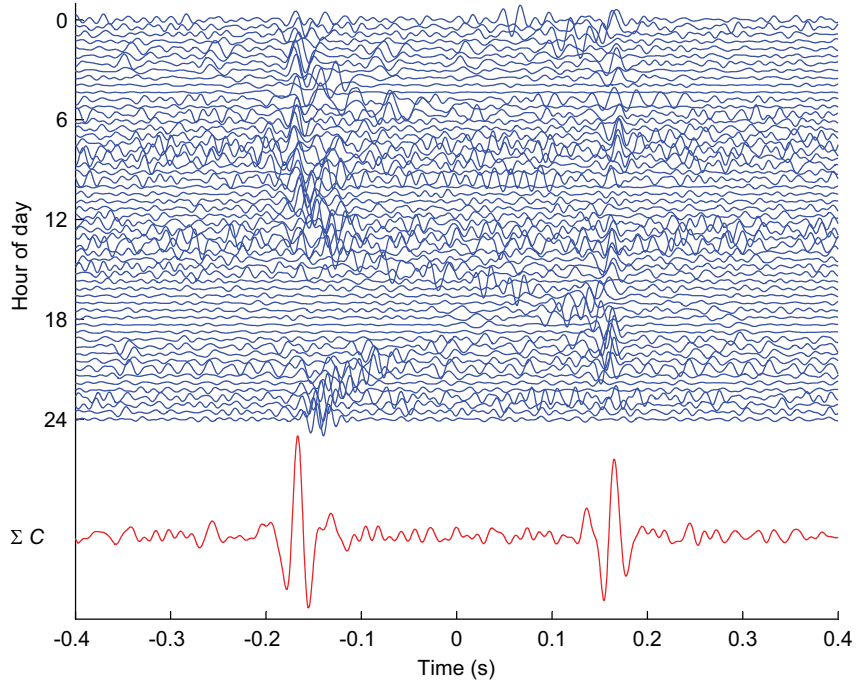
Figure 6.13: Short time cross-correlations of 6 minutes and 24 seconds for H-30 and H-5 ship dominated ambient noise data as a function of time of September 2. The sum of the entire day's cross-correlations, $\sum C$, is shown underneath.

fire location, and EGFAs from a ship dominated ambient noise field. It was shown that the EGFAs from all source configurations yield direct arrival time estimates that match well with the simulated direct arrivals, though the stationary ship arrival times were slightly early. The ability to determine surface reflected arrivals was more variable between techniques, with the towed source and ship dominated ambient noise giving the best results. Due to their greater complexity, the surface-bottom reflected arrivals between H-32 and the VLA hydrophones were not as well determined.

In order to more fully understand how the EGFA evolves for each source configuration, the cross-correlations for one source pair, H-30 and H-5, were analysed as a function of time, and the experimental active source cross-

correlations were compared to those obtained from simulations. The empirical and simulated summed cross-correlations were then compared to the simulated source shaded Green's function, and differences between these were explained with reference to the theory in Chapter 3. The experimental and simulated cross-correlations showed many of the same characteristics.

Although it is the direct path arrivals estimated from the ship dominated ambient noise that will be applied to problems of array monitoring and localisation in Chapter 7, direct arrival times estimated from the EGFAs of active source configurations could also potentially be used for similar purposes.

Chapter 7

Practical Applications of Travel Time Estimates

The experimental results presented in Chapter 5 show that although correct amplitudes are difficult to obtain, the arrival structure of the Green's function between two hydrophones can be accurately approximated from the summed cross-correlation of ship dominated ambient noise. This chapter describes how the inter-hydrophone travel time estimates extracted from this ambient noise ocean acoustic interferometry data can be used for two practical applications:

1. diagnosis of a problem of channel switching on an ocean hydrophone array, and

2. array shape determination.

A significant proportion of the work in this chapter has been accepted for publication in JASA-EL [86].

7.1   Introduction

As a result of Tropical Storm Ernesto, large sea state and wind conditions started to develop during the evening of September 1. All experimental

activities then ceased until September 3. The acoustic arrays remained operative throughout this period. Analysis of experimental data recorded on the 20 hydrophone horizontal portion of SWAMI32 after the storm revealed that several channels in the array had switched.

The term *channel switching* refers to the event where signals from a given hydrophone that were previously recorded on a certain channel, are subsequently recorded on a different channel; *hydrophone* refers to the physical transducer in the array; and *channel* refers to the recording medium where the data from a hydrophone were stored. Hydrophone and channel numbers matched upon deployment of the array, as shown in Figure 7.1(b), but not after the channel switching occurred, as shown in Figure 7.1(c)–(d).

This chapter describes how ambient noise cross-correlation of array data from during the storm are used to diagnose a problem of channel switching that occurred between hydrophone pairs. When channel switching occurs, a set of two given channels begin to record data from a different pair of hydrophones, and hence the inter-hydrophone travel time, determined from cross-correlation of the signals, will change. The estimated travel times, and specifically changes therein, are used to determine on which channel the data from each hydrophone are being recorded at any given time during the day. Consequently, the time and manner in which the channel switching occurs is ascertained.

In addition to the channel switching, it was noticed that travel times of acoustic data recorded on the SWAMI32 array showed inconsistencies with the given array geometry; difference in travel times from any given source to horizontal line array (HLA) hydrophone pairs were consistently less than expected. Cross-correlations of data recorded on SWAMI52 and Shark during this time period yielded travel time estimates that did not vary significantly from that expected for the given geometry. It was therefore hypothesised that the HLA hydrophones were spaced more closely than the *a priori* specifications, most likely due to the HLA not lying in a straight line on the seafloor. Travel times extracted from day long September 2 ambient

146

noise cross-correlations of SWAMI32 data, with the channel switching taken in to account, are in agreement with this hypothesis.

Direct path travel times are estimated for all hydrophone pairs 12–32 (12 is in the vertical line array (VLA) approximately 2 m above the bottom, and 13–32 form the bottom-mounted HLA). Inter-hydrophone distances are then estimated assuming constant sound speed, which is a valid assumption since hydrophones 12–32 are all at or near the ocean bottom where the SSP does not change significantly. Using the travel times, an inversion for array geometry is performed using the MATLAB® nonlinear least squares algorithm, which uses a subspace trust region method for nonlinear minimisation [87, 88].

7.2 Diagnosis of channel switching

7.2.1 Analysis of recorded data

The SWAMI32 array, the geometry of which is shown in Figure 7.1(a), has a 256-m long horizontal portion consisting of 20 hydrophones with tapered spacing.

Preliminary analysis of acoustic data (see Section 7.2.2) from active sources collected throughout the experiment shows that switching of channels occurred. Since no active source experiments were undertaken during the storm, further details of the switching could not be determined using traditional techniques; however, ambient noise cross-correlations (see Section 7.2.3) show when, and in what manner, the switching occurred.

7.2.2 Active sources

Data from both broadband pulses and combustive [89] sound sources show that before the storm the signals recorded on each channel correspond to the correct hydrophones shown in the *before switching* configuration of Figure 7.1(b). The signal from a broadband 1100–2950 Hz energy pulse,
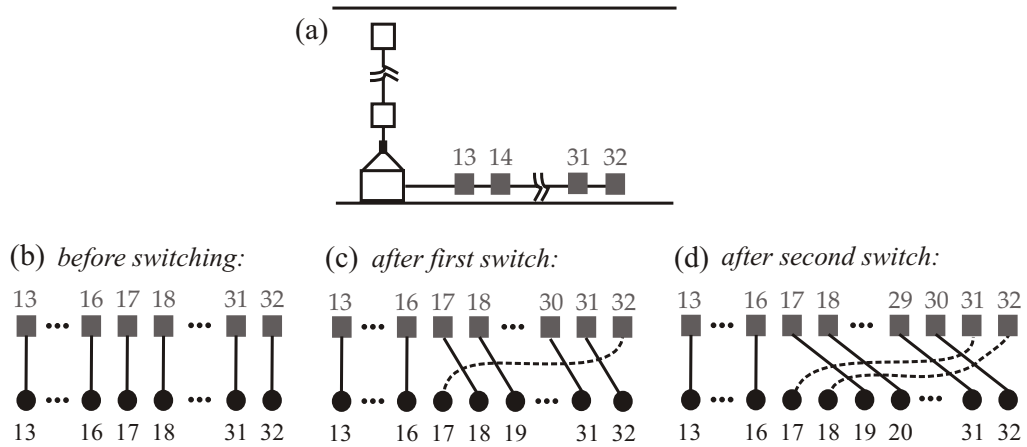
Figure 7.1: (a) Array geometry. (b)–(d) Schematics showing the hydrophone-channel connections: (b) at deployment, (c) after the first switch, and (d) after the second switch.

recorded at 6:04 Z on August 31, 21° from the HLA axis, and 1385 m from the closest hydrophone (hydrophone 32), was projected to the on-axis direction. The envelope of the projected signal received by each HLA channel, where channels are directly interchangeable with hydrophone numbers for this case, is shown in Figure 7.2(a). The time of arrival is plotted relative to the first direct arrival. Several reflected arrivals are observable on each channel at times later than the direct. As expected, each arrival is received first by the channel corresponding to the closest hydrophone, channel 32, and the arrival times increase as the channel number decreases. The time interval between arrivals on each channel increases due to tapering of the array spacing.

After the storm, data from both linear frequency modulated (LFM) sweep sources and combustive sound sources indicated that some switching of channels had occurred. The match filtered signal from a 1100–2900 Hz 1–s duration LFM source, held 10 m below the water surface, recorded at 14:40 Z on September 3, on-axis with the HLA, and 150 m from the closest hydrophone, is shown in Figure 7.2(b). The signals recorded on each channel no longer correspond to the correct hydrophones. The data from
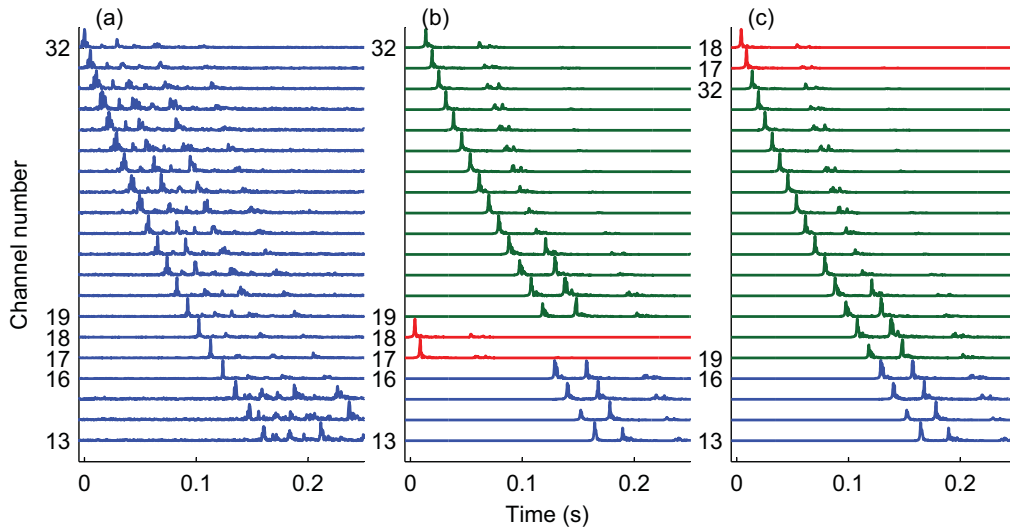
Figure 7.2: Envelope of the signal recorded on each channel from active source testing (a) before the storm at 6:04 Z on August 31, and (b) after the storm at 14:40 Z on September 3. (c) Signal envelope from after the storm with channels re-sorted. Channels 14–15 and 20–31 are unnumbered, but are in order between 13 and 16, and between 19 and 32, respectively.

hydrophones 31 and 32 are recorded on channels 17 and 18 respectively, and the data from hydrophones 17–30 are all recorded 2 channels higher than expected, as shown in Figure 7.1(d). Figure 7.2(c) shows the data after re-sorting the channels so that the data from hydrophones 13 through 32 are in order. The arrival times and the manner in which the shape of the envelope evolves are consistent, which shows that data recorded after switching of the channels occurred are reliable (i.e., acoustic data from each hydrophone are still being recorded).

The channels did not revert to their original configuration, but retained the configuration of Figure 7.1(d) for the remainder of the experiments. It is not known what caused the switches to occur, though possible reasons have been hypothesised. The HLA was connected, through a junction box, to a VLA with a large float at the top (5 m below the sea surface). It is possible that large waves which broke over the VLA float during the storm could have tugged on connecter cables, resulting in the propagation

of an impulsive source down the cable and subsequent damage to the cable connections. It is also possible that the problem was not mechanical, but occurred in the electrical systems of the junction box in which the data were stored. Unfortunately these and other hypotheses could not be tested as the array is owned by a non-local organisation and therefore physical access could not be gained.

7.2.3   Ambient noise cross-correlations

As described in Section 2.2.2, the cross-correlation between two hydrophones, denoted A and B, as a function of time delay, τ, is defined as

$$C_{AB}(\tau) = \int_{-\infty}^{\infty} p_A(t) p_B(t + \tau) dt, \qquad (7.1)$$

where p is the pressure recorded at each hydrophone, and t is time. It has been shown [8, 15] that the arrival-time structure of the Green's function, G, between hydrophones A and B, defined as the signal which would be received at A given a unit impulsive source at B, can be extracted from the time-derivative of the ocean noise cross-correlation function:

$$\frac{\partial C_{AB}(\tau)}{\partial t} \simeq - \left[G_{AB}(t) - G_{AB}(-t) \right]. \qquad (7.2)$$

The raw cross-correlation, rather than its time derivative, is often used as an approximation to the Green's function [25, 56], and for a finite bandwidth signal this can be a good approximation, since the cross-correlation and its derivative closely resemble one another. However, if exact arrival times are desired, the cross-correlation time derivative should be employed, as this corrects for the $\pi/2$ phase difference between the raw cross-correlation arrival peak, and that of the Green's function [15].

Ship dominated 20–100 Hz noise was recorded throughout the day that Tropical Storm Ernesto passed through (see Chapter 5). After preprocessing the data, cross-correlation periods of 6:24 min (6 minutes and 24 seconds), which corresponds to the length of a single data file, were used. Since the width of the cross-correlation waveforms are narrow relative to travel times

between receivers, it is sufficient to consider the raw cross-correlations for the purpose of determining which channels are recording data from which hydrophones. Due to the short cross-correlation times, peak amplitudes of the post-processed data were prone to temporal bias from high amplitude directional sources (see Section 5.6). However, even if the source field is not evenly distributed, the time of the cross-correlation peak between the hydrophones increases with distance. Examination of the raw cross-correlations over the entire day revealed three main findings: (a) the channel switching occurred in two steps; (b) a short time period during which each switch occurred can be estimated; and (c) the raw signals, and hence the signal cross-correlations, recorded for a significant time period before and after each switch, exhibit high levels of noise on the higher channels.

Cross-correlations from times prior to and after each switch occurred are shown in Figure 7.3(a)–(d). Figure 7.3(a), which depicts the cross-correlations starting at 7:07:37 Z, shows that the channels are in order, and the cross-correlation peaks correspond to a move-out velocity of approximately 1500 m/s, as expected. The cross-correlations of data starting at 7:14:01 Z are shown in Figure 7.3(b). These show an anomaly in the signal recorded by channel 17. The signal does show a small peak at the expected move-out velocity; however, the major peak occurs at a time of just under 0.2 s, which is the expected cross-correlation time for channel 32. The signals recorded on channels 18 through 32 exhibit major peaks corresponding to those expected for one channel lower than their assigned values. These results suggest that channel 17 switched within the period 7:17 Z±3 min, the relative peak amplitudes indicating that the switch was closer to the start of this time period. Note that the cross-correlations for channels above 17 exhibit high levels of noise. High noise levels were, in fact, observed on channels 18–32 for a two hour period surrounding this time (5:40–7:40 Z), suggesting that the channel switching and the increase in noise are linked. The hydrophone-channel connections after this first switch are shown in Figure 7.1(c).
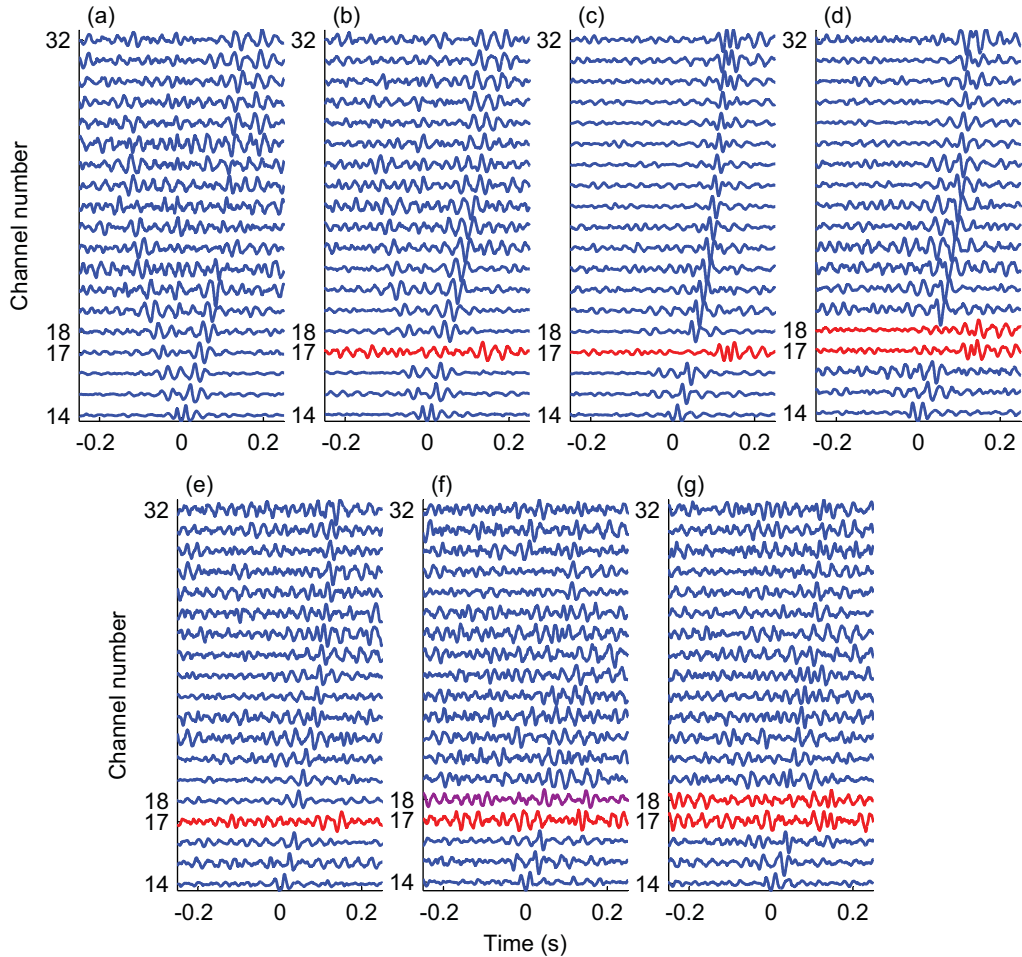
Figure 7.3: Short time cross-correlations (6:24 min) between channel 13 (first HLA hydrophone) and all other channels from the time period surrounding the first switch (a) 7:07:37 Z and (b) 7:14:01 Z, and from the time period surrounding the second switch (c) 12:08:40 Z and (d) 12:15:05 Z. (e)-(g) 20 s long cross-correlations at 12:14 Z for times (e) 20–40 s, (f) 30–50 s, and (g) 40–60 s.

Results of cross-correlation of data starting at 12:08:40 Z are shown in Figure 7.3(c). Channel 17 is still the only channel to have switched. Cross-correlations of data immediately following this, starting at 12:15:05 Z are shown in Figure 7.3(d). These cross-correlations suggest that channel 18 has also switched. Now channels 17 and 18 are recording data from hydrophones 31 and 32, and channels 19–32 are recording data from two hydrophones less than their number. This configuration matches the 'after switching' description of Section 7.2.2 that is depicted graphically in Figure 7.1(d) and Figure 7.2(b). Cross-correlations with higher numbered channels exhibit less noise than during the first switch, and high noise levels were only observed for a few minutes around the time of the second switch.

Cross-correlations over shorter time periods were employed to narrow down the time window during which the second switch occurred. Cross-correlations of 20-s duration were calculated from 12:08:40–12:21:29 Z. Three results from the minute of 12:14 Z are shown in Figure 7.3(e)–(g): (e) 20–40 s, (f) 30–50 s, and (g) 40–60 s. Due to the shorter duration of the cross-correlation time, the cross-correlations exhibit high noise levels; however the peak arrivals can still be observed. The first cross-correlation, Figure 7.3(e), suggests that channel 17 has switched but 18 has not. The second cross-correlation, Figure 7.3(f), is the least clear, but suggests that the switch occurs during this time period, since both the true and delayed arrival are seen. The third cross-correlation, Figure 7.3(g), also exhibits the true and delayed arrival; however, the delayed peak dominates, suggesting that the switch occurred closer to the start of the cross-correlation period. The likely time interval during which the second channel switching occurred is thus 12:14:45 Z$\pm$5 s.

Once the switch times had been determined, data from the entire day of September 2 were correlated in three time segments: (a) immediately before either switch, (b) after the first switch but before the second switch, and (c) immediately after the second switch. The channels were re-sorted so that the data from hydrophones 13 through 32 were in order, and then

plotted as a function of distance from hydrophone 13 in Figure 7.4(a)–(c). The cross-correlation peaks are seen to increase linearly in time with distance along the array, which is in agreement with the results previously described. The noise levels are lower than those in Figure 7.3 due to the longer cross-correlation periods. The envelopes of the time-derivatives of the cross-correlation functions, which, as previously mentioned, relate to the arrival times between hydrophones, are shown in Figure 7.4(d)–(f), corresponding to data in Figure 7.4(a)–(c) respectively. The simulated travel times between hydrophones, which were determined using OASES [49], are also shown. The envelope peaks are in agreement with the direct arrival, and also with the surface reflected arrival at greater distances. The surface reflected arrival is not seen at closer distances due to the steeper grazing angles, which are accompanied by greater bottom loss.

Figures 7.3 and 7.4 show only the cross-correlations between channel 13 and other channels. Comparisons between all channels can be made by considering the peak of the envelope of the time-derivative of the cross-correlation function, which, as previously mentioned, corresponds to the arrival times between hydrophones when the noise sound field is isotropic.

The arrival time corresponding to the envelope peak of the noise cross-correlation time-derivative is plotted for all channel pairs in Figure 7.5 for three 6:24 min periods at (a) 2:20 Z, (b) 10:55 Z, and (c) 23:15 Z. These correspond to time periods well before the first switch occurred, in between when the two switches occurred, and after the second switch occurred. During the high noise level time periods surrounding the switch times, a clear peak in the gradient envelope was difficult to obtain, and therefore the time periods used here are well away from the switch times. The correlation times of Figure 7.5 give additional support to the findings that the channel switching occurred in two steps. Figure 7.5(c) shows peak times that are less than those shown for (a) and (b). This suggests that the noise field at 23:15 Z is dominated by off-axis directional energy in the data (see Section 5.6). However, as mentioned in Section 7.2.3, even if the source field
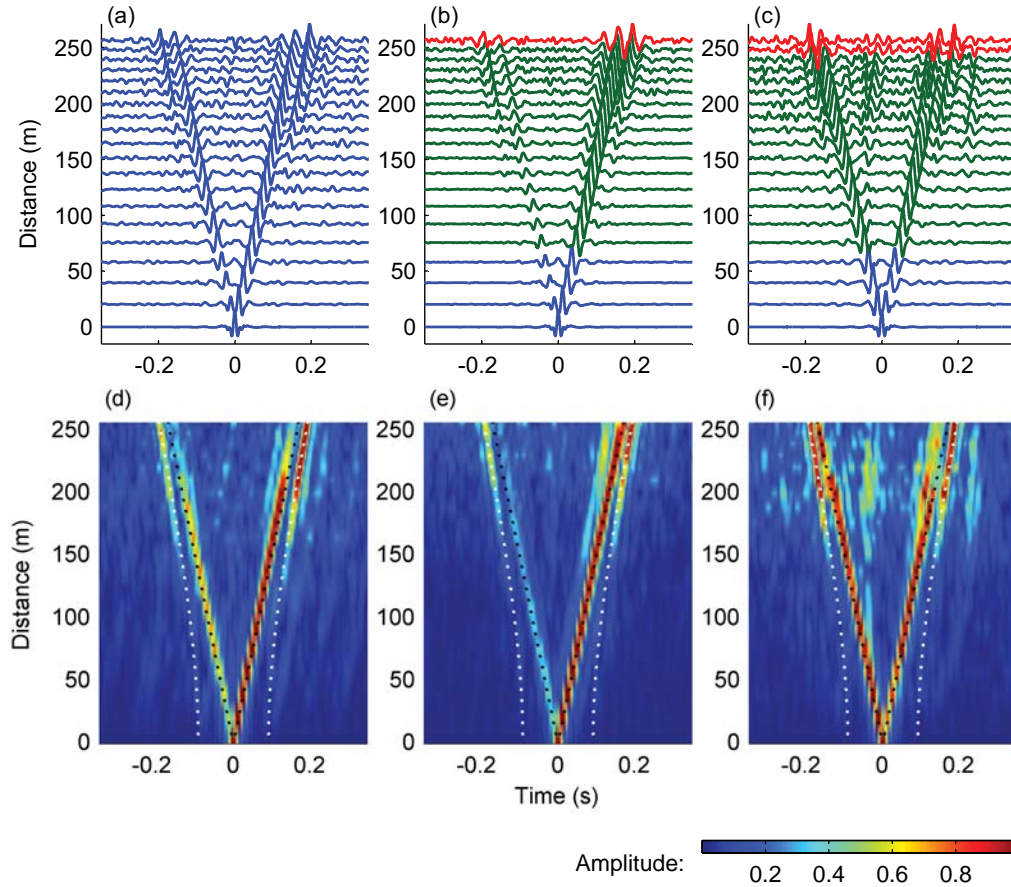
Figure 7.4: (a)–(c) Cross-correlations between channel 13, the first HLA hydrophone, and all other channels after re-sorting the channels, plotted as a function of distance from hydrophone 13: (a) before, (b) between, and (c) after the switches. (d)–(f) Normalised envelopes of the cross-correlation function time-derivatives, with simulated direct (black dotted lines) and surface reflected path travel times (white dotted lines): (d) before, (e) between, and (f) after the switches.
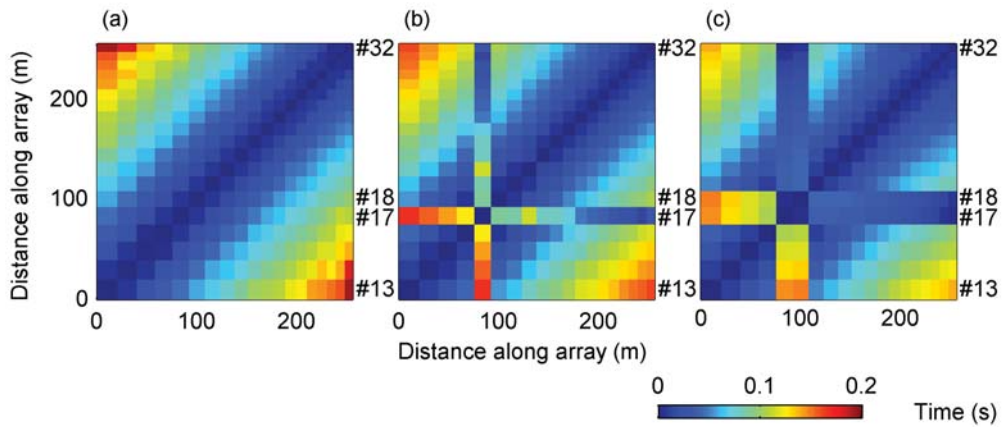
Figure 7.5: Arrival time as a function of distance from the first HLA element (hydrophone 13), from (a) before the first switch at 2:20 Z, (b) after one channel has switched at 10:55 Z, and (c) after both channels have switched at 23:15 Z.

is not evenly distributed, the time of the cross-correlation peak between the hydrophones increases with distance, and therefore only the relative times are important.

7.2.4 Conclusion

Results from active source experiments near the SWAMI32 array prior to and after the day Tropical Storm Ernesto passed through the region showed that some channels had switched during the storm.

Ambient noise cross-correlation of data from September 2 was successfully employed to determine more information about the nature of the channel switching. The cross-correlation analysis suggested that the switching occurred in two distinct stages. The change that occurred at each stage was identical; the channel that was recording the data of hydrophone 17 started recording data from hydrophone 32, and the channels recording data from hydrophones 18 through 32 all moved down one hydrophone. The inferred time intervals during which each switch happened were narrowed down to the periods 7:17 Z±3 min and 12:14:45 Z±5 s. Elevated noise levels were ob-

served on each channel for a significant time period surrounding each switch. The noise levels were especially high during the first switch, making it difficult to narrow down the time of the switch to as small a time window as was obtained for the second switch. Longer time period cross-correlations from before, between, and after the switches occurred, supported the findings. With the channels re-sorted to the correct hydrophones, the cross-correlation function time-derivative envelopes showed accurate arrival time structure.

7.3   Array shape estimation

Estimation of array shape from travel times and other acoustic data has previously been performed using discrete sources [90–92]. Either an active source or ship noise at approximately known locations is used. If exact source locations are not known, the inversion algorithm can invert for both source and receiver positions. Inputs for the inversions generally consist of source-receiver travel times, *a priori* estimates of the source and receiver geometry, and estimated errors in travel times and geometry, as well as other assumptions such as the array elements being able to be approximated by a smooth function.

Sabra *et al.* [27] developed a 2 dimensional algorithm (all receivers must be located on the same horizontal plane, allowing for an isovelocity assumption) for array element self-localisation from ambient noise cross-correlations. Their methods were experimentally shown to be effective for HLA hydrophone localisation, and as such, form a basis for the methodology presented here.

All the HLA elements as well as the lowest VLA element are considered here. The VLA element is included so that the location of the HLA relative to the VLA can be estimated also. Velocity changes near the bottom of the water column are negligible and therefore the isovelocity assumption remains valid.

7.3.1 Inter-hydrophone travel times

Correlations of SWAMI32 20–100 Hz September 2 data were performed following the methodology of Chapter 5. Travel times, $T_{i,j}$, between hydrophones i and j were then estimated as the peak of the empirical Green's function approximation envelope.

7.3.2 Inversion algorithm for array element localisation

The fundamentals of a generic inversion process are included in Appendix C. The array element inversion process presented here attempts to determine an array geometry with inter-hydrophone travel times that best match the measured travel time estimates.

The bottom of the VLA is chosen as the origin, and the 20 HLA elements, which are all assumed to be at a constant depth, are parameterised in 2D by their distance and azimuth from the first element. The VLA element is parameterised by its height from the seafloor.

The model vector of unknown parameters is

$$\mathbf{m} = [h_1, d_2, ..., d_M, \theta_2, \theta_3, ..., \theta_{M-1}]^{\mathrm{T}}, \tag{7.3}$$

where $M = 21$ is the number of elements in the array, h_1 is the height of the VLA hydrophone above the seafloor, d_j is the distance from the origin to element j, and θ_j is the azimuth relative to the two ends of the array (i.e., $\theta_M = 0$). The inversion therefore seeks to estimate $2M - 2$ unknowns.

The observed data vector:

$$\mathbf{T} = [T_{1,2}, T_{1,3}..., T_{1,M}, T_{2,3}, ..., T_{M-1,M}]^{\mathrm{T}}, \tag{7.4}$$

consists of $M(M-1)/2$ terms.

The array is *a priori* assumed to be straight. The *a priori* estimate of the unknown parameters is therefore $\mathbf{m_{ap}} = [l_2, ..., l_M, 0, ..., 0, c_0]^T$, where l_j is the pre-experiment measured hydrophone separation.

The inversion seeks to minimise the difference between the measured travel times and those computed from the model vector, whilst simulta-

neously ensuring that the resulting hydrophone locations lie on a smooth spline.

The computed travel times are

$$\mathbf{T_{cal}} \quad = \quad \left[\frac{\sqrt{|d_2 e^{i\theta_2}| + h_1^2}}{c_0}, ..., \frac{\sqrt{|d_k e^{i\theta_2}| + h_1^2}}{c_0}, ..., \frac{\sqrt{|d_M e^{i\theta_2}| + h_1^2}}{c_0}, \right. \tag{7.5}$$

$$\left. \frac{|d_3 e^{i\theta_k} - d_2 e^{i\theta_j}|}{c_0}, ..., \frac{|d_k e^{i\theta_k} - d_j e^{i\theta_j}|}{c_0}, ..., \frac{|d_M e^{i\theta_M} - d_{M-1} e^{i\theta_{M-1}}|}{c_0} \right]^T. \tag{7.6}$$

The travel time differences should be weighted by the inverse of the uncertainties of the measured times. This is done by pre-multiplication with the diagonal regularisation matrix:

$$\mathbf{W_1} = diag \left[w_{1,2}, w_{1,3}..., w_{1,M}, w_{2,3}, ..., w_{M-1,M} \right], \tag{7.7}$$

where $w_{j,k}$ are uncertainty weightings for each observation data. If the uncertainty is assumed to be a constant number of samples independent of the hydrophone pair, then the difference between the observed travel times, $\mathbf{T}$, and the computed travel times, $\mathbf{T_{cal}}$, should be equally uncertain regardless of hydrophone pair. Unity regularisation weighting was therefore used.

The first objective function to be minimised is

$$\Phi_1 \quad = \quad [\mathbf{W_1}(\mathbf{T} - \mathbf{T_{cal}})]^T [\mathbf{W_1}(\mathbf{T} - \mathbf{T_{cal}})] \tag{7.8}$$

$$= \quad [(\mathbf{T} - \mathbf{T_{cal}})]^T [(\mathbf{T} - \mathbf{T_{cal}})]. \tag{7.9}$$

The second consideration of the inversion is the shape of the array. The *a priori* assumption is that the array is straight. The inversion therefore seeks to minimise the difference in azimuth between straight lines connecting successive elements.

The change in azimuth vector between the lines connecting two successive elements is

$$\Delta\Theta = [\Delta\theta_2, ..., \Delta\theta_j, ..., \Delta\theta_{M-1}]^T, \tag{7.10}$$

where

$$\Delta\theta_j = \text{phase}(d_{j+1} e^{i\theta_{j+1}} - d_j e^{i\theta_j}) - \text{phase}(d_j e^{i\theta_j} - d_{j-1} e^{i\theta_{j-1}}). \tag{7.11}$$

Unity regularisation weighting is applied. The smoothness objective function is therefore

$$\Phi_2 = [\Delta\Theta]^T[\Delta\Theta]. \tag{7.12}$$

The objective function to be minimised is the weighted sum of Φ_1 and Φ_2:

$$\Phi = \Phi_1 + \alpha\Phi_2 = [(\mathbf{T} - \mathbf{T_{cal}})]^T[(\mathbf{T} - \mathbf{T_{cal}})] + \alpha[\Delta\Theta]^T[\Delta\Theta], \tag{7.13}$$

where α is the Lagrange multiplier that governs the relative importance of the observed travel times and the array smoothing.

The array geometry is estimated as that which minimises the objective function, Φ.

7.3.3 Application to data

The array element localisation algorithm was applied to the travel times obtained from the JD245 ambient noise cross-correlations. Minimisation of the objective function was achieved using the MATLAB® nonlinear least squares algorithm, which uses a subspace trust region method for nonlinear minimisation [87, 88].

Since the least-squares algorithm attempts to minimise all travel time differences, it can be susceptible to bias from outliers. The six largest values were therefore rejected for each calculation of the objective function (stability was checked and results using rejection of 5–20 largest values showed negligible variation).

Lower and upper limits on inter-element spacing were set to half and twice the *a priori* values. The large upper bound was used because inversion results yielding distances greater than the *a priori* data would have suggested a problem with either the data or the algorithm. The distances calculated from the inversion were; however, consistently about 5% less than the *a priori* values, which is consistent with the expectation that the hydrophones were spaced more closely.

The inverted element location results are show in Figure 7.6, along with the *a priori* locations. The *a posteriori* geometry supports the original
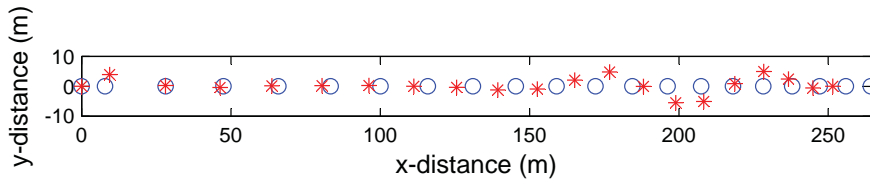
160

Figure 7.6: Array element locations: *a priori* (circles) and *a posteriori* results from non-linear least squares travel-time inversion (asterisks).

hypothesis that the HLA was not lying in a straight line. Results using estimates of the unknown parameters $\mathbf{m_{ap}}$ that are different to the *a priori* geometry converge to the same *a posteriori* geometry. The *a posteriori* geometry results were observed to match travel times from all active sources at known locations near the array better than the *a priori* straight line geometry.

7.3.4 Conclusion

An inversion algorithm for array element localisation, that used inter-hydrophone travel times estimated from ship dominated ambient noise cross-correlation, was successfully applied to SWAMI32 hydrophone data. The curved *a posteriori* array shape matched travel times from active sources at known locations better than the *a priori* shape, supporting the original hypothesis that the array was not lying in a straight line

Chapter 8

Conclusion

Knowledge of the ocean acoustic Green's function can be used to determine information about the ocean environment through which acoustic transmission between two points takes place. There exists limited prior literature that addresses ocean acoustic interferometry, that is, Green's function approximation from cross-correlation of sound in the ocean. The work in this thesis aimed to further the understanding of ocean acoustic interferometry in a shallow water oceanic waveguide.

8.1 Summary of thesis findings

This thesis focussed upon ocean acoustic interferometry using two source types: active sources, and ship dominated ambient noise. Theoretical descriptions, simulated and experimental results (using data collected on the outer New Jersey Shelf during the Shallow Water 2006 sea trials), as well as two practical applications of ocean acoustic interferometry, were presented.

A stationary phase argument was used to theoretically describe the relationship between the summed cross-correlations from a line of active sources, and the Green's function between two hydrophones. Three active source configurations were considered: vertical and horizontal line sources, located in the same vertical plane as two hydrophones; and a horizontal

163

hyperbolic source with its asymptote at a location horizontally midway between two hydrophones. The theory and simulations for the vertical line source presented here were shown to be in agreement with a modal approach presented by others, and results for cross-correlations of towed horizontal line and hyperbolic sources were shown to be in agreement with theoretical work on cross-correlations of wave generated ocean noise, modelled as a horizontal plane of sources, as well as horizontal lines of seismic surface sources. The three source configurations were compared and their advantages and disadvantages highlighted. Due to its close proximity, signals from the source column were shown to have minimal attenuation, but the source column geometry did not account for the modal continuum of the ocean sediment. The towed source scenarios were shown to suffer from intrinsic stationary-phase contributions from cross-correlations between a wave that initially undergoes a surface reflection and one that does not. The hyperbolic source was shown to have the advantage of being able to approximate the Green's function between a physical receiver and a virtual receiver; however, unlike the other two configurations, the theory assumed range independence and therefore is not applicable in some environments.

Experimental data were collected during the Shallow Water 2006 experiments. It was shown that the ocean environment was characterised by a strong thermocline and significant spatiotemporal variability. The resulting direct path acoustic field was shown to include multi-path interference, with high sensitivity to ocean variations. It was therefore difficult to extract accurate reflection coefficient information from the acoustic data. It was decided that sediment properties needed as input data for cross-correlation simulations would therefore be better estimated from available nearby sediment grab sample data.

Cross-correlations of ocean noise in the ship dominated 20–100 Hz frequency range were used to determine empirical Green's function approximations (EGFAs). Since ship noise is generated at discrete locations, long cross-correlation periods were required to give sufficient averaging for the

emergence of the Green's function. For a frequency band with sufficient levels of coherent noise, different time and frequency domain normalisation methods yielded similar cross-correlation results. A major reason for this is the spatial averaging of the noise field that occurred when noise from many ship tracks were recorded. Direct, surface reflected, and bottom-surface reflected travel times between hydrophones were determined from the EGFA envelopes for three L-shaped arrays, and agreed well with simulated data. Summing the cross-correlations between equi-spaced horizontal line array (HLA) hydrophone pairs was shown to increase the signal-to-noise ratio. Analysis of temporal variations in the cross-correlations confirmed that the signal was generally dominated by only one or two sources at any one time. Cross-correlations obtained from data recorded during Tropical Storm Ernesto were shown to be clearer than those obtained before and after the storm. This was due to a combination of a reduction in high energy discrete sources (most ships left the area during the storm), and an increase in overall sound levels. High amplitude discrete sources were not averaged out during cross-correlation, and could therefore result in EGFA peaks at times earlier than the inter-hydrophone travel times. Removal of a dominant discrete source was shown to improve the EGFA by removing a corresponding high amplitude peak at a time less than the inter-hydrophone travel time.

Cross-correlations were examined for experimental data obtained from two of the three active source configurations discussed in the theory: a source lowered vertically, and a source towed horizontally. Hyperbolic source data were collected but not analysed in detail because they showed less resemblance to the acoustic Green's function than the other two source configurations. The results were compared with cross-correlations from the ship dominated noise field, and also with cross-correlations of noise generated during a source lowering event by the ship from which the source was being controlled. The active source data EGFAs were shown to have higher signal-to-noise ratios than the EGFAs from ship noise. This was due to the

higher levels of coherently propagating noise that resulted from the close proximity of the source, and the even source distribution over the active source line integrals. The differences between the EGFAs and simulated Green's functions were explained with reference to theory and simulations by considering the results for a single hydrophone pair. Approximation of direct paths were shown to be consistently good for each source configuration. Surface reflection paths were shown to be more accurate for hydrophones with a greater horizontal separation, and the towed source and ship dominated ambient noise were shown to be best for determining surface reflected arrivals overall.

Two practical applications of ocean noise cross-correlation were detailed: the diagnosis of a problem with a multichannel hydrophone array, and array element self-localisation. Results obtained from active source measurements revealed that signals from several hydrophones, which were recorded on certain channels before the storm, were subsequently recorded on different channels after the storm. Noise cross-correlation of data recorded during the storm showed when, and in what manner, this channel switching took place. The inferred intervals during which each switch occurred were narrowed down to two time periods, 6 minutes and 10 seconds long respectively. With the channels re-sorted to match the correct hydrophones, the cross-correlation function time-derivative envelopes were shown to give accurate arrival time structure at all times before, during, and after the storm. In addition to the channel switching, it was noticed that differences in travel times from any given source to HLA hydrophone pairs were consistently less than expected for the assumed geometry. It was therefore hypothesised that the HLA was not lying in a straight line on the seafloor. Travel times extracted from day long ambient noise cross-correlations of data, with the channel switching taken into account, were used in a non-linear least squares inversion to estimate array geometry. The resulting curved array geometry provided more consistent acoustic travel times from active noise sources than the assumed straight line array geometry.

In conclusion, the findings discussed in this thesis increase the understanding of Green's function approximation from cross-correlation of sound in the ocean. This thesis provided a theoretical and practical understanding of Green's function estimations for two noise types: active sources and passive ship-dominated ambient noise. Cross-correlations of the ship noise, which has the advantage of no additional source instrumentation being required, were shown to be of good quality when the source distribution was fairly evenly distributed, but degenerated when the incoming source field was directionally biased. Cross-correlations of the active source signals, which have the advantages of higher frequencies, giving sharper arrival peaks, as well as controllability and continuous monitoring, were shown to have a higher signal-to-noise ratio than the ambient noise cross-correlations, but suffer from spurious arrivals that are intrinsic to the source geometry.

Two examples of how travel time information extracted from Green's function estimates can be applied to a practical situation were also provided in this thesis. By better understanding the effects of both source geometry and ocean environment on Green's function approximation, it is anticipated that in the future more of the information obtained from ocean acoustic interferometry will be able to be successfully used for practical purposes.

Much of the work presented in this thesis has either been published or submitted for publication by the author in both journals and conference proceedings, as listed in Appendix D.

8.2   Recommendations for future work

The active source experiments detailed in this thesis were the first known set of experiments of their type conducted for the purpose of ocean acoustic interferometry. Much has been learnt from analysis of the collected data, and as such, it would be beneficial to investigate in more detail the SNR of the cross-correlated waveforms as a function of environmental, geometric, and experimental parameters. The first recommendation for future work

presented here concerns such an investigation.

In addition, it would be of useful to be able to perform additional active source experiments using the information that has been learnt from the original experimental design and the subsequent analysis of data. Two of the recommendations for future work presented here concern the collection of additional active source data, and the further analysis of current data if additional information becomes available.

Travel times obtained from cross-correlations were shown to be useful for practical applications. However the work presented in this thesis provides just one step towards the larger goal of using Green's function approximations to determine environmental characteristics such as water column and seafloor properties. It is anticipated that with further development of ocean acoustic interferometry techniques, more information can be obtained from the empirical Green's function approximations and used for practical purposes. Two of the recommendations for future work therefore concern cross-correlation analysis at lower frequencies, and over greater distances than considered within this thesis, with the ultimate goals of determining and monitoring sediment properties.

8.2.1 Effect of various parameters on SNR

A detailed investigation of how certain parameters affect the signal-to-noise ratio of the cross-correlation would be helpful to understand the ocean acoustic interferometry technique more completely, and the results from such an investigation would be advantageous for the design of future experiments. Parameters that could be investigated include noise time-series bandwidth, sensor separation, recording time, attenuation, and ocean fluctuations (in particular changes in waveguide depth due to wave activity, and changes to the sound speed profile). This investigation would, at first, need to be performed by variation of each parameter individually through theory and simulation rather than experimentation, as the uncertainties and changes in the ocean environment would make it difficult to experimentally

focus upon changes in only one parameter at a time.

8.2.2   Additional source lowering experiments

If the opportunity to perform additional at-sea experiments in calmer waters becomes available, then another source lowering experiment should be performed, this time lowering over the whole water column depth. This should remove the spurious arrivals that exist due to gaps in the source distribution at the waveguide top and bottom. The more stable ocean environment will also increase the resolution of the results. Several source lowering experiments at various distances from the array should be performed. This will enable the formulation of a better understanding of the cross-correlation amplitudes and their relationship to the experimental geometry. Analysis of the amplitudes of peaks in the unsummed cross-correlations could then potentially be used to estimate surface and bottom reflection properties. This will require a multi-variable inversion method because reflection properties have angular dependence, the sea surface is not stationary, and the seafloor may be range-dependent. Multiple source lowering distances and calmer conditions would make this task more feasible than it would be for the current data set.

Lowering a source over the water column takes a time period that is long with respect to the time scale of changes in the ocean environment due to processes such as wave activity. It would therefore be desirable to perform an experiment that is geometrically similar to the lowering experiment, except that a vertical array of closely spaced sources spanning the water column is used instead. This would allow for the approximation of short-term Green's functions and would also be useful for monitoring how the Green's function approximation changes over time, and for relating these changes to short time scale processes such as wave activity, and medium time scale processes such as tidal effects.

8.2.3 Experimental hyperbolic source

The theory governing cross-correlation for a horizontal hyperbolic source was presented in Section 3.3. Experimental data from a source towed along hyperbolic paths were collected during the SW06 experiments on the same day and using the same towed source as the horizontal towed straight line source described in Chapter 6. The ship travelled along two hyperbolic paths, as shown in Figure 8.1. Hyperbolic path 1 was designed such that its focal point coincided with hydrophone 30, its apex was at a point midway between hydrophones 30 and 28, and its asymptotic origin was at a point midway between hydrophone 30 and the vertical line array (VLA). Hyperbolic path two also had the same focal point and asymptotic origin, but the apex was chosen to be midway between hydrophones 30 and 16.

The accuracy of the source track is critical around the hyperbola apex. An accurate track was able to be obtained due to the dynamic positioning capabilities of the ship, as shown in Figure 8.2.

Preliminary analysis of hyperbolic source data cross-correlations revealed that they showed less resemblance to the acoustic Green's function between two points than the straight line horizontal source tow. A contributing reason for this is likely to be that the hyperbolic configuration assumed range independence, but the environment was actually range dependent. Hence, if an accurate mapping of the local water column depth and sediment properties could be obtained, then the results from the straight line towed source and hyperbolic towed sources could potentially be used to examine sensitivity of the method to range-dependence.

In addition, if the opportunity to perform at-sea experiments in a range independent environment were to become available, the straight line and hyperbolic source tows could be repeated. This would give a better idea of how factors other than range dependence affect the results obtained using a hyperbolic configuration rather than a straight line tow.
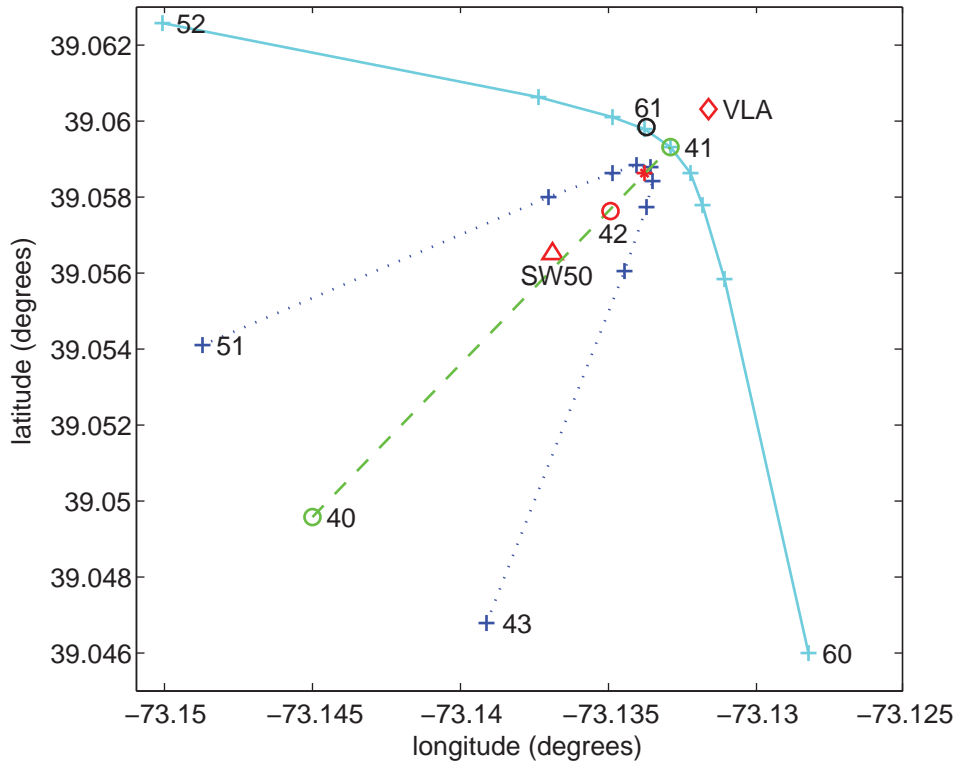
Figure 8.1: Mid-frequency SWAMI32 towed source tracks: straight (green dashed), hyperbolic path 1 (dark blue dotted), and hyperbolic path 2 (light blue). Numbered markers are waypoint numbers, 'VLA' is the location of the vertical portion of the SWAMI32 array, and the horizontal portion of the array extends from the VLA to the point marked by an asterisk.

8.2.4 Cross-correlations at seismic frequencies

Due to the maximum array lengths of 465 m, the minimum frequency of the acoustic data used in this thesis was 20 Hz. The SWAMI32, SWAMI52, and Shark arrays were located several kilometres apart. Cross-correlation of data from hydrophones located on separate arrays could therefore be performed at seismic frequencies. Each array had a different sampling frequency, but this would not present a problem as all data would be downsampled to the same frequency. There were also timing errors of several seconds between the arrays. Corrections for this would need to be made

171

Figure 8.2: Hyperbolic tracks were achieved using dynamic ship positioning. The desired navigation path is entered into the system (blue path) and the actual ship position, shown as grey images, is mapped over time. The ship and navigation path are to scale.

before data cross-correlation.

Data from three stationary sound sources could be used to correct for the timing errors. The stationary sources were active for the first few minutes of every half hour throughout the time the arrays were deployed:

1. *National Research Laboratories* (NRL) 300 Hz linear frequency modulated signal, Bandwidth of BW=60 Hz;

2. *Woods Hole Oceanographic Institute* (WHOI) 224 Hz phase encoded signal, BW=16 Hz; and

3. WHOI 400 Hz phase encoded signal, BW=16 Hz.

The location of these sources relative to the hydrophone arrays is shown in Figure 8.3. The signals emitted by these sound sources were loud enough to be received clearly at each hydrophone array and therefore timing errors could be corrected for using the arrival times, at each array, of the signals emitted by each sound source using a triangulation method.

The greater distances and hence lower frequencies used by cross-correlating between arrays would potentially allow the current study of
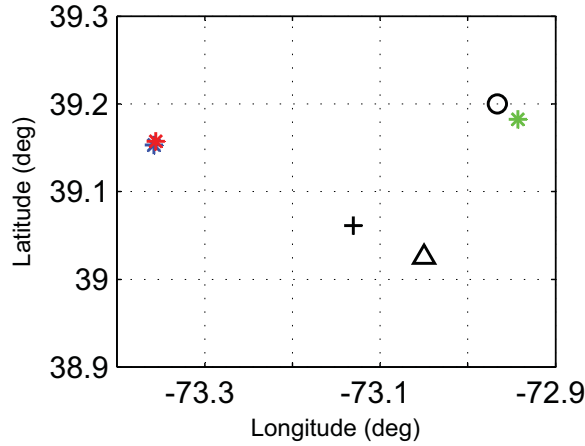
Figure 8.3: Locations of fixed sound sources: NRL 300 Hz (green asterisk), WHOI 224 Hz (blue asterisk), and WHOI 400 Hz (red asterisk); and locations of L-shaped hydrophone arrays: SWAMI52 (circle), Shark (triangle), and SWAMI32 (cross).

body waves (i.e., waves travelling within the ocean waveguide) to be extended to surface waves travelling along the seafloor-sediment interface.

8.2.5 Cross-correlations for monitoring gas hydrates

A gas hydrate sea-floor observatory has recently been installed over a one-kilometre-diameter carbonate/hydrate mound in the Gulf of Mexico Mississippi Canyon Block 118. The location of this canyon block is shown in Figure 8.4. The observatory includes four 400-m horizontal line arrays, each with 16 hydrophones, nested in a 1000 m cross configuration, as shown in Figure 8.5. The large array aperture allows for analysis of lower frequency data than that considered in this thesis.

Cross-correlation of low frequency wave generated seismo-acoustic ambient noise can therefore be used to determine travel times between pairs of sensors in the HLA. Sub-bottom paths will likely be more easily extracted from this lower frequency seismic data. Analysis of long term changes in

NOTE: This figure is included on page 174 in the print copy of the thesis held in the University of Adelaide Library.

Figure 8.4: Location of Mississippi Canyon Block 118 (MC118), (source: McGee *et al.* [93]).

sub-bottom travel times between sensors can potentially be used to determine when changes have occurred in the materials through which the noise travels. This passive monitoring technique will hopefully lead to an understanding of how fluids migrate and affect the formation of hydrates within the carbonate/hydrate mound.

The seismo-acoustic monitoring technique is a large project within itself and will require several steps:

1. Using existing techniques and codes, an automatic processing technique that removes strong events, and filters and spectrally equalises

NOTE: This figure is included on page 175 in the print copy of the thesis held in the University of Adelaide Library.

Figure 8.5: Gas hydrate sea-floor observatory in Mississippi Canyon Block 118 (source: McGee [94]).

the noise data, will need to be developed and fine-tuned depending upon the characteristics of the noise data collected.

2. Subsequent to initial data analysis, adjustments to the physical experimental set-up will need to made. In particular, adjustments to array design and sampling time intervals may be needed.

3. Noise sources will likely include distant storms, local breaking waves, ships, seismic exploration, and biological sources. Identification and classification of these sources will be necessary as each source type will have different characteristics and propagation paths and will therefore affect the cross-correlated data in different ways. Spatial, azimuthal, and temporal variations in the noise strength will also need to be interpreted in terms of strength and direction for each type of noise source. This step will likely be the most difficult and time consum-

ing; an accurate understanding of spatio-temporal characteristics is vital since otherwise it will not be known whether any changes in the cross-correlation are due to changes in the carbonate/hydrate mound structure or whether they are simply due to changes in source characteristics.

4. Temporal stability of the technique will then need to be assessed and changes will need to be made until a monitoring capability can be demonstrated.

5. Once a monitoring capability has been demonstrated, results will need to be compared with those from high-resolution seismic data for the site to assess the accuracy of the developed technique.